공학박사학위논문

A study on particle deposition and clogging dynamics of colloidal suspensions in complex flow

복잡 유동장 내 콜로이드 현탁액의 입자 적층 및 유로 막힘 거동에 관한 연구

2023년 8월

서울대학교 대학원

화학생물공학부

김 대 연

A study on particle deposition and clogging dynamics of colloidal suspensions in complex flow

복잡 유동장 내 콜로이드 현탁액의 입자 적층
및 유로 막힘 거동에 관한 연구

지도교수 안 경 현

이 논문을 공학박사 학위논문으로 제출함
2023년 8월

서울대학교 대학원
화학생물공학부
김 대 연

김대연의 공학박사 학위논문을 인준함
2023년 8월

위 원 장 _____ (인)

부위원장 _____ (인)

위 원 _____ (인)

위 원 _____ (인)

위 원 _____ (인)

Abstract

A study on particle deposition and clogging dynamics of colloidal suspensions in complex flow

Dae Yeon Kim
School of Chemical and Biological Engineering
The Graduate School
Seoul National University

The aim of this dissertation is to investigate the process of particle accumulation in particulate suspensions under complex flow and the consequent clogging of the flow path, as well as to identify the underlying mechanisms that govern the accumulation phenomenon in various flow environments, such as membrane separation processes, with the ultimate goal of developing effective mitigation strategies. Although numerous studies have employed microfluidics to understand and mitigate membrane fouling, most have focused on phenomenological studies of multi-pore structures, neglecting the more fundamental unit of single pores and their deposition environment. To address this research gap, the unit structures of dead-end flow and cross-end flow filtration, which are representative filtration methods of the membrane separation process, are simplified into contraction and T-shaped microchannel respectively to investigate particle deposition and pore clogging. The attachment and detachment forces that affect the actual particle deposition and

clogging, including particle-particle, particle-wall, and hydrodynamic interaction due to flow, are considered and a comprehensive research methodology is constructed.

First, the phenomenon of particle deposition in contraction channels under different salt concentrations and flow conditions using a suspension of polystyrene particles dispersed in an aqueous glycerol solution is studied. The size of the colloidal interaction is controlled by varying the salt concentration, while the hydrodynamic interaction is regulated through the control of the flow rate. The results show that the particle deposition pattern in the contraction channel is changed based on the salt concentration. For colloidal interactions with a strong attraction, particle deposition is predominantly observed in the upstream region of the channel, while deposition occurs mainly in the downstream region for repulsive colloidal interactions. Additionally, as the flow rate increases, the deposition proceeds more rapidly, and the amount of deposition in the upstream region increases. Image processing and pressure drop measurements are used to quantification of deposition, and the observed phenomena are explained by comparing the relative magnitudes of colloidal and hydrodynamic interactions. The study concluded that the progression of deposition is determined by the relative magnitude of the forces due to each interaction in the upstream and downstream regions, and the change in the hydrodynamic force due to the size of the colloid also has an effect.

Second, the particle deposition phenomenon according to the flow conditions in the T-shaped channel is studied. In the T-shaped channel, the effect of stress acting as a detachment force is focused. The stress is changed by the fluid viscosity and flow rate, and the fluid viscosity is controlled by the glycerol concentration. It is confirmed that the particle deposition process proceeds step by step in the order of edge deposition, deposition growth, and pore clogging. During this process, a rolling

phenomenon in which the particles seem to roll on top of the deposited aggregates and an agglomerate breakup phenomenon in which the aggregates are separated are repeated. Depending on the magnitude of the applied stress, it is determined whether or not the pore is blocked. To quantify particle deposition, the pore blockage ratio and the deposition area ratio are defined. Through this, the existence of critical stress that causes pore clogging is confirmed. At a stress smaller than the critical stress, the clogging is reached, and vice versa. The value of the critical stress is validated through a dimensionless number expressed as the ratio of the hydrodynamic drag force and the interaction force between particles. The stress values in the range of equal magnitudes of the two forces almost coincided with the critical stress values. Through this, it is concluded that the stress due to flow can have a very important effect on particle deposition and clogging, and that the relative ratio of attachment and detachment force can be used as an index to predict pore clogging.

This dissertation contributes to a comprehensive understanding of the pore clogging by examining the phenomenon of particle deposition under a complex flow through the balance of various forces. The consideration and analysis methodology for particle clogging in unit structure channels conducted in this study is expected to provide a basis for research on clogging in complex fluids and various unit structure channels. Based on this, it is expected that an effective particle deposition and clogging reduction strategies can be established.

Keywords: Particle deposition, pore clogging, fouling, dead-end filtration, cross-end filtration, contraction, T-shaped channel, suspensions, aggregation, microfluidics

Student Number: 2017-29046

Contents

List of Figures

List of Tables

Chapter 1. Introduction

1.1. General introduction

The flow through confined geometries is a widely studied environment due to its industrial significance and ubiquitous nature. Complex fluids comprising of polymers, particles, and various additives experience intricate flow fields such as contractions, expansions, bends, crossflows, and separations in unit processes such as coating, jetting, spraying, and mixing used in semiconductor, battery, and polymer processing. The elasticity of the polymer can cause flow instability, such as vortex and secondary flow [1, 2], in the complex fluid flowing through these geometries. The interaction between the pipe wall and particles can lead to deposition, and sometimes agglomeration [3-5], of particles in the flow. Moreover, the deposited particulate agglomerates may be separated due to the hydrodynamic stress induced by the flow, and large aggregates in the fluid may break up into several pieces [6]. Thus, research on the flow of complex fluids is crucial for designing and improving the efficiency of slurry transportation and storage processes.

Among the various unit processes, membrane filtration is commonly used to maintain or enhance fluid dispersibility. Foulants, foreign substances or large agglomerates in the fluid, must be removed in the intermediate stage to avoid major defects in the final product. Membranes with numerous pores eliminate the foulants in particle suspension. However, continuous transport of the suspension often leads to membrane fouling or clogging, which ultimately reduces process performance and productivity. Various temporary strategies such as back flow reversal, back pulsing, and patterned membrane have been proposed as solutions to fouling and clogging [7,

8]. However, to address the fouling and clogging issues fundamentally, it is necessary to identify the clogging mechanism.

A membrane is a complex structure composed of numerous pores with pore sizes ranging from several nanometers to several tens of micrometer. To investigate the clogging mechanism at the macro scale, it is necessary to identify the clogging mechanism at the micro scale, particularly at the single-pore level. Microfluidics has been widely utilized to observe the clogging of suspensions directly at the single or multi-pore level and to implement various flow conditions. The pore of the membrane can be categorized into two fundamental geometries based on the filtration method: dead-end flow filtration and cross-end flow filtration. Dead-end flow filtration can be represented as a contraction where the flow path sharply narrows, while cross-end flow filtration can be expressed as a T-shaped configuration where one flow is divided into two flows.

Numerous previous studies have investigated the clogging mechanism in microchannel-simulated membranes, and the findings are largely divided into three categories. The clogging mechanisms of microfluidic channel flow are sieving caused by size exclusion [9], bridging or arching caused by multiple particles reaching the pore simultaneously [10], and continuous particle deposition, which is classified as aggregation-induced clogging [11, 12]. Aggregation-induced clogging, which has been the subject of intensive research recently, is a mechanism affected by the interaction between particles, the interaction between particles and walls, and the hydrodynamics due to flow, with various complex factors involved. Previous studies have independently observed the effect of each factor in the geometry simulated by multi-pore, with a focus on colloidal interactions. However, it is essential to comprehensively consider the hydrodynamic stress applied due to the flow and

identify the clogging due to particle deposition. Also, before proceeding with a practical study on the clogging issue, additional hydrodynamics in a fluid with added elasticity must be considered.

Therefore, this thesis systematically studies particle deposition of particulate suspension flowing in contraction geometry and T-shaped geometry, which are the most fundamental geometries of membrane filtration, and resulting clogging by comprehensively considering colloidal interaction and hydrodynamics stress.

1.2. Objective and outline of the thesis

This thesis aims to understand the fundamental mechanism of particle deposition on contraction and T-shaped geometries which are the most fundamental flows of membrane filtration. In addition, contraction and T-shaped geometry are pivotal unit geometries in a slurry transport system where the particle deposition and pore clogging frequently occur. The mechanism of particle deposition and clogging is systematically studied by considering the colloidal interaction between particle and wall and the hydrodynamic effect.

In chapter 2, the effect of colloidal interaction and hydrodynamic stress on particle deposition in the contraction channel is studied. In this chapter, the clogging dynamics in single contraction geometry is investigated by controlling the surface property of the particle and flow condition. Microfluidic observation is conducted to investigate particle deposition in a contraction microchannel where polystyrene suspension is injected as a feed solution. The particle deposition is quantified using the images taken using a CCD camera and the pressure drop across the microchannel is also measured.

In chapter 3, the particle deposition and clogging in the T-shaped channel is studied. In this chapter, the mechanism of particle deposition in cross-flow is investigated using polystyrene particles dispersed in the glycerol solution. The flow rate and glycerol concentration are systematically controlled to analyze the effect of hydrodynamic stress on the clogging mechanism. Through flow visualization and image processing, the study identifies the step-by-step process of particle deposition and accumulation. Furthermore, this chapter suggests that there is critical stress that inhibits particle deposition and prevents pore clogging, and this stress is determined

by the balance between the hydrodynamic force and the colloidal interaction force.

In chapter 4, concluding remark is presented that summarizes the results presented in the previous chapter and discusses the significance and value of the research conducted.

Chapter 2.

Particle deposition and clogging in the dead-end flow through a 4:1 contraction microchannel

2.1. Introduction

Material processing can be understood as the 'transport phenomena of complex fluid' [13] in a wide range of industries such as petrochemicals, semiconductors, batteries, biotechnology, and pharmaceuticals. In these processes, materials flow through various confined geometries such as pipes, nozzles, filters, and membranes [14-28]. A colloidal suspension flowing in such a confined geometry often causes clogging, which is an undesirable phenomenon because it degrades process performance and causes various flow problems (e.g., unpredictable deformation of the flow field, increased residence time, and vortex formation) [28]. To understand the clogging mechanism, microfluidics has been widely employed in previous studies because the operational conditions (e.g., geometrical parameters or flow conditions) are easily controlled and direct observations of clogging dynamics are possible [29].

The clogging mechanism in the microchannel flow can be classified into three types: sieving, bridging, and aggregation, according to the ratio between the pore size and particle size [28]. Sieving is the simplest clogging mechanism that excludes particles or aggregates larger than the pore size [30, 31]. However, even if the pore size is larger than the particle size, clogging can occur due to bridging and aggregation. Bridging is a phenomenon in which arch-shaped blockage occurs at the pore entrance when the number of particles that simultaneously pass through the pore exceeds the

number of particles that can pass through the pore at one time [10]. Aggregation is a phenomenon in which aggregates grow and clogging occurs due to the successive deposition of particles and is determined by the interplay of hydrodynamics and surface interactions [11, 31, 32].

Among the factors affecting the clogging mechanism, researches on colloidal interactions have been extensively conducted. Bacchin *et al*.[33] studied the effect of colloidal interaction on the filtration cake shape by controlling the suspension stability. Sendekie *et al*.[34] investigated the filtration process in terms of surface interaction and hydrodynamics. Both studies were performed with a well-defined and strong confinement geometry where the colloidal interactions between the particle and wall are predominant. Agbangla *et al*.[35] employed a numerical simulation to understand particle deposition according to the hydrodynamics and colloidal interactions at the pore entrance. Delouche *et al.* [36, 37] analyzed the difference in the clogging process according to the size and shape of the aggregates. Besides, the fouling in the straight channels has been studied both experimentally[3, 38] and numerically[39, 40].

Most of the clogging studies were conducted in multi-pore channels, however, it is difficult to identify the fundamental process of clogging in the multi-pore due to the overlapping influences from the adjacent pores. Although it is necessary to study the clogging mechanism in a single-pore geometry to overcome this limitation, it has rarely been studied compared to the multi-pore system. Kim *et al*.[41] investigated the correlation between the rheological properties and the clogging mechanism by observing the single-pore clogging that occurs only below a critical shear stress. Dersoir *et al*.[42-44] carried out experimental studies on progressive clogging using a fast confocal microscope. They determined the different steps of the clogging

process at the pore through careful observation of aggregate growth dynamics. In addition, they confirmed that the clog formation could be affected by the shape of the pore entrance and the relative ratio between pore and particle size. However, in these single-pore studies, the colloidal interactions were not sufficiently considered, leading to a limitation in the comprehensive understanding of the clogging dynamics.

In this study, we investigate the clogging dynamics in terms of the colloidal interaction and hydrodynamic stress in a single-pore system through microfluidics and image analysis. In contrast to previous studies, we focus on partial clogging caused by particle deposition. Microfluidic observation is performed using polystyrene suspensions in a PDMS-fabricated contraction channel where the changes in deposition behavior are monitored by controlling the salt concentration and flow rate. The width of the channel is large enough to observe the partial clogging at the contraction. The particle deposition behavior is analyzed and quantified. Meanwhile, the effect of hydrodynamic stress on clogging is confirmed by calculating the wall shear stress in the channel. In addition, the effect of colloidal size on particle deposition is further analyzed by controlling the agglomerate size with sonication.

This chapter is organized as follows: Section 2.2 presents the details of the materials, visualization setup, and flow conditions. Section 2.3 provides the clogging behavior observations. The colloidal interaction potential is calculated according to the salt concentration while the clogging behavior is analyzed through image processing and pressure drop measurements. Moreover, the mechanism of particle deposition is discussed. Section 2.4 summarizes the results and provides concluding remarks.

2.2. Experimental

2.2.1. Materials

In this study, destabilized polystyrene (PS) suspensions are prepared as a working fluid. A glycerol aqueous solution is used as a suspending medium and the glycerol concentration is fixed at 60 wt% in all samples. Monodisperse polystyrene (PS) latex (solid% = 4 %, surface charge density = 18.2 μC/cm^2, Invitrogen, USA) with a size of 1.5(±0.05) μm is used where the particle concentration is fixed at 0.1 wt%. PS particles have a negative surface charge (ζ-potential ~ -32 mV, measured by particle size analyzer ELS-Z, Otsuka Electronics, Japan) due to the carboxyl groups on the surface, resulting in a well-dispersed state by electrostatic repulsion. Before experimentation, the polystyrene latex is exposed to sonication for more than 1 minute to break down the agglomerates, if there are any. To control the surface property, NaCl is added at a varying concentration of 1, 10, and 100 mM. As the salt concentration is less than the critical coagulation concentration (CCC ~ 0.4 M), no sedimentation occurs. For sample preparation, glycerol (Glycerin, Daejung Chemicals & Metals Co., Ltd., Korea) and deionized water are well mixed for 30 minutes, and then NaCl is dissolved for 1 hour. Then, the polystyrene latex exposed to sonication is added and mixed with a magnetic stirrer (180 rpm) for 24 hours. The viscosity of the prepared sample is about 9.3 cP at all shear rates, which suggests the Newtonian behavior. The viscosity is measured by using a rotational rheometer, AR-G2 (TA instruments, USA) with a 60 mm parallel plate at 25 °C (**Fig. 2.1**). The formulation of the samples and the flow conditions used in this study is provided in **Table 1**.

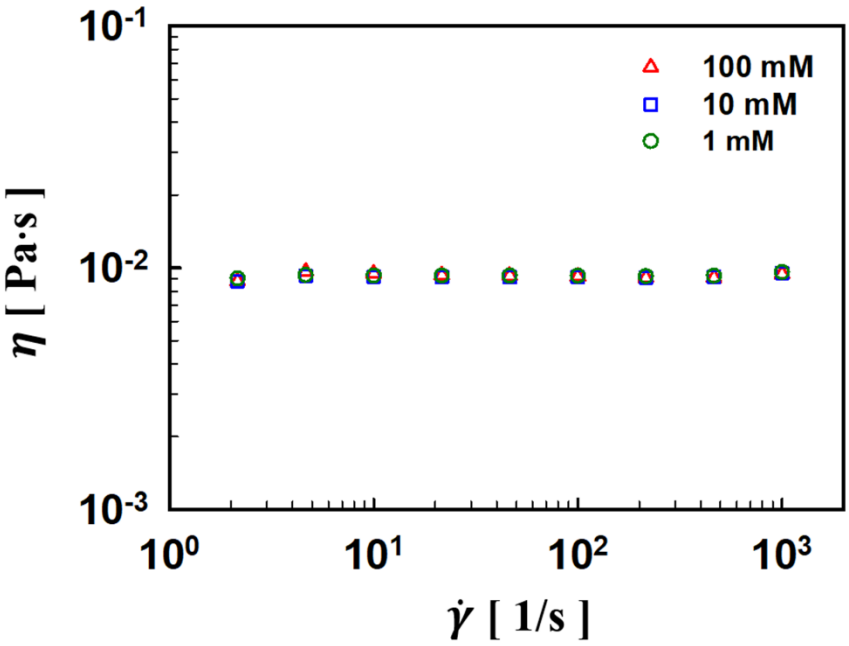

Fig. 2.1. Shear viscosity (η) of sample with various NaCl concentration as a function of the shear rate ($\dot{\gamma}$).

Table 1. Formulation of the samples used and flow conditions

Glycerol [wt%]	PS [wt%]	NaCl [mM]	η [cP]	Q [ml/hr]
60	0.1	1, 10, 100	9.3 ± 0.2	0.3, 0.7, 1.2

2.2.2. Microfluidics and visualization setup

The experiments are performed in a contraction microchannel (**Fig. 2.2a**) where the upstream length of the channel (W_u), downstream length of the channel (W_d), and height of the channel (h) are 180, 45, and 100 μm, respectively. The contraction ratio of the channel is 4. The microchannel is fabricated by using a SU-8 mold and poly(dimethylsiloxane) (PDMS, Sylgard 184A, Sewang Hitech Silicone, Korea). The PDMS and curing agent (Sylgard 184B, Sewang Hitech Silicone, Korea) are pre-mixed at a ratio of 10 to 1, and the mixture is poured onto a SU-8 mold for pre-baking. Then, the channel is baked in an oven at 80 ℃ overnight. Detailed information on the fabrication process can be found in reference [41]. Using the fabricated PDMS microchannel, the particle deposition behavior in the contraction region is observed by the inverted microscope, IX-71 (Olympus, Japan), and a highly sensitive CCD camera (Hamamatsu, Japan) (**Fig. 2.2b**). A syringe pump, PHD 4400 (Harvard apparatus, USA), is used to inject flow into the channel. The pressure drop is also measured using a pressure sensor, uPS0800 (LabSmith, USA), which is mounted between the syringe and the channel inlet. All the flow paths, except for the PDMS channel, are connected through Tygon tubing.

Three flow rate conditions — 0.3, 0.7, and 1.2 ml/hr — are used in the microfluidics experiments. Channel swelling does not occur significantly within the flow condition used. As the flow rate increases, the differential pressure drop within the channel increases linearly. However, it should be noted that local swelling may not be reflected. For convenience, the flow rate conditions of 0.3, 0.7, and 1.2 ml/hr are labeled as q0.3, q0.7, and q1.2, respectively. All samples are injected into the channel at a constant flow rate using a syringe pump and the images of particle deposition at

the contraction region are recorded every minute through the CCD camera. The pressure drop is measured immediately after flow injection. All flow tests are conducted at least 3 times under each condition to secure reproducibility. The Reynolds number (Re $= \rho \bar{V}_d D_h / \eta = 2\rho Q / (W_d + h)\eta$, the ratio of inertial force to viscous force, where ρ is the fluid density, $\bar{V}_d = Q / W_d h$ the average velocity, D_h the hydraulic diameter, and η the shear viscosity.) falls in the range of 0.2 – 0.7 and the Stokes number (St $= 2\rho_d R^2 \bar{V}_d / 9\eta W_d$, where ρ_d is the particle density, and R is the radius of the particle) is calculated in the order of O(10^{-19} – 10^{-18}), which means that the particles follow the streamlines very closely.

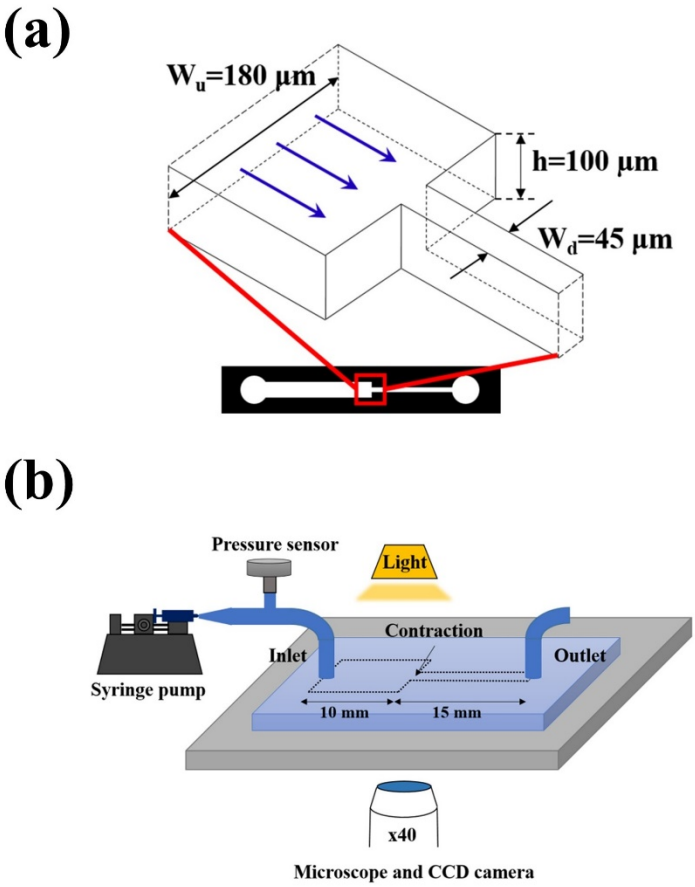

Fig. 2.2. (a) A projected view of the 4:1 contraction microchannel (W_u : upstream width of the channel, W_d : downstream width of the channel, h : height of the channel). Flow direction is indicated by blue arrows. (b) Schematic of the microfluidic observation system.

2.3. Results and Discussion

2.3.1. Sample characterization

Fig. 2.3 shows the images of the samples at different salt concentration. The size of the particles and agglomerates is determined as the Feret diameter (d_F) which is the longest distance between two points along the subject boundary. The size distribution of each sample is presented in **Fig. 2.4**. In the case of 1 mM, most of the particles are well dispersed in the form of primary particles at an average size of about 1.5 μm (**Fig. 2.3a**). As the salt concentration increases, agglomerates are formed due to particle aggregation, where the average agglomerate size is about 10(±11.7) μm for 10 mM (**Fig. 2.3b**) and about 20(±16.6) μm for 100 mM (**Fig. 2.3c**). The difference in the agglomerate size can be explained with the DLVO potential, which quantitatively represents the colloidal interaction. The DLVO potential is calculated as follows.

Particle-particle and particle-wall interaction potentials are evaluated as the sum of the van der Waals interaction and electrostatic double layer interaction [20].

$$U_{total} = U_{vdW} + U_{el} \tag{1}$$

Particle-particle DLVO potential ($U_{total,p-p}$) is calculated with the distance between two identical spherical particles

$$U_{vdW,p-p} = -\frac{A}{6}\left[\frac{2}{{l_1}^2 - 4} + \frac{2}{{l_1}^2} + \ln\left(1 - \frac{4}{{l_1}^2}\right)\right] \tag{2}$$

$$U_{el,p-p} = \frac{32\pi\varepsilon R k_B^2 T^2 \gamma_0^2}{Z^2 e^2} \exp(-\kappa R(l_1 - 2)) \tag{3}$$

$$\gamma_0 = \left[\exp\left(\frac{Ze\psi_0}{2k_B T}\right) - 1\right] \Big/ \left[\exp\left(\frac{Ze\psi_0}{2k_B T}\right) + 1\right] \tag{4}$$

where $U_{vdW,p-p}$is the van der Waals attraction potential, $U_{el,p-p}$ the electrostatic double layer potential, A the Hamaker constant, $l_1 = d_1/R$ (d_1 the center-to-center interparticle distance, R the radius of the particle), ε the medium permittivity, k_B the Boltzmann constant, T the absolute temperature, e the elementary charge, ψ_0 the surface potential, κ the inverse of the Debye length, and Z the counter-ion charge.

Particle-wall DLVO potential ($U_{total,p-w}$) is calculated according to the interaction between a spherical particle and an infinite flat surface.

$$U_{vdW,p-w} = -\frac{A}{6}\left[\frac{1}{l_2 - 1} + \frac{1}{l_2 + 1} + \ln\left(\frac{l_2 - 1}{l_2 + 1}\right)\right] \tag{5}$$

$$U_{el,p-w} = \frac{64\pi\varepsilon R k_B^2 T^2 \gamma_0^2}{Z^2 e^2} \exp(-\kappa R(l_2 - 1)) \tag{6}$$

The parameters used for particle-wall DLVO interaction are the same as in particle-particle interaction. l_2 is d_2/R, in which d_2 is the particle center-to-surface distance. The parameters are provided in **Table 2**.

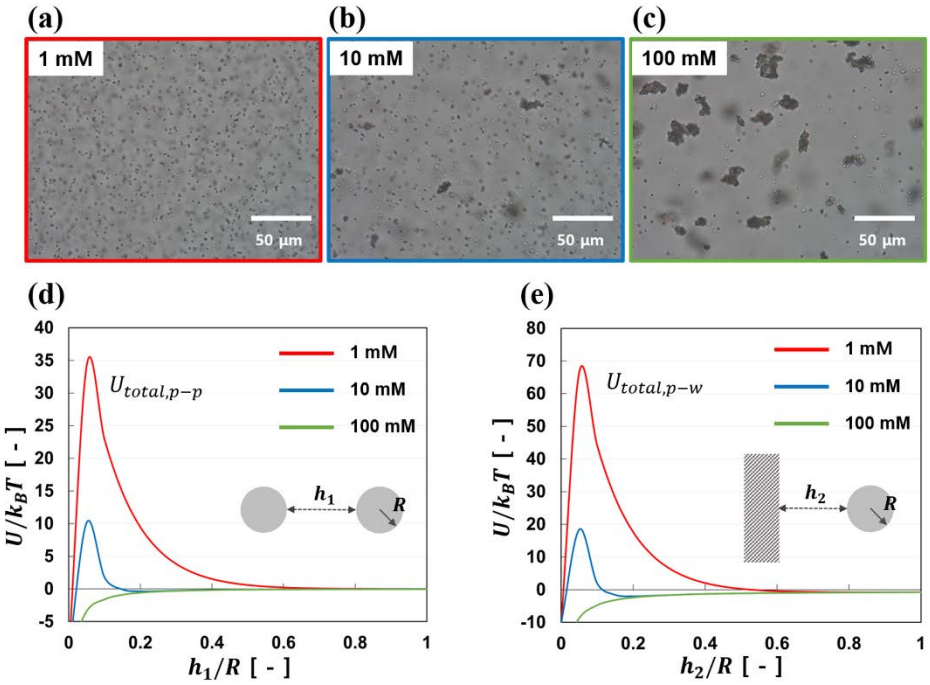

Fig. 2.3. Microscope images of the samples at different salt concentrations: (a) 1 mM, (b) 10 mM, (c) 100 mM. (d) The particle-particle and (e) the particle-wall DLVO interaction potential. h_1 is the surface-to-surface distance between the particles. h_2 is the surface-to-surface distance between particle and wall.

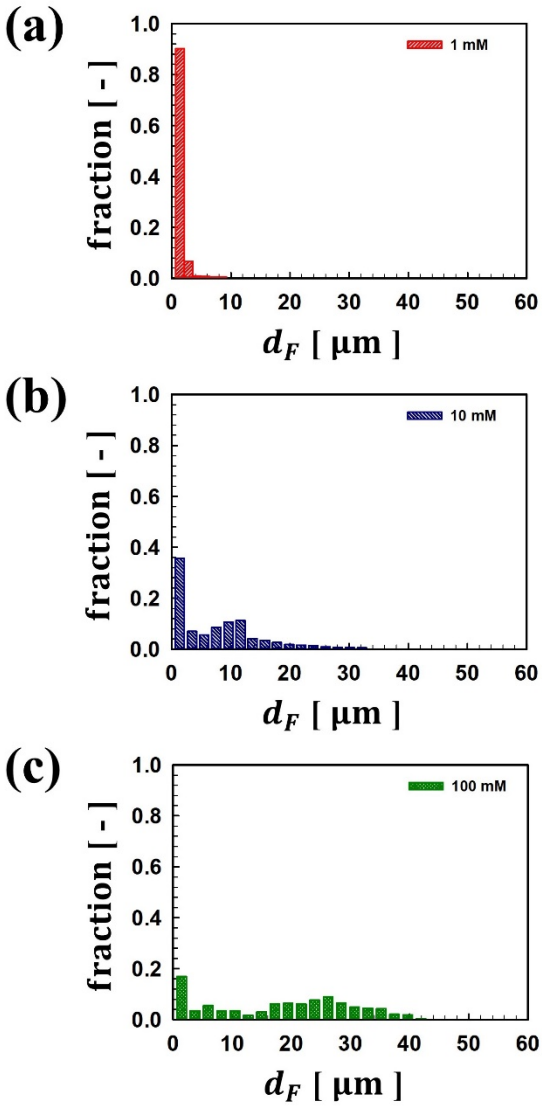

Fig. 2.4. The size distribution at different salt concentration: (a) 1 mM, (b) 10 mM, and (c) 100 mM. The size of the particles and agglomerates is based on the Feret diameter and measured by image processing. At least 3,000 objects are measured for size distribution.

Table 2. DLVO parameters

Parameter	Description	Value
R	Radius of particle [μm]	0.75
ε	Medium permittivity [F/m]	5.34×10^{-10}
T	Absolute temperature [K]	293.15
k_B	Boltzmann constant [J/K]	1.4×10^{-23}
A	Hamaker constant [J]	1.3×10^{-20}
ψ_0	Surface potential [mV]	-32
e	Elementary charge [C]	1.602×10^{-19}
Z	Counter-ion charge [-]	1
κ^{-1}	Debye length [nm]	8.4 (1 mM) 2.6 (10 mM) 0.8 (100 mM)

Fig. 2.3d and **Fig. 2.3e** show the calculated particle-particle and particle-wall interactions, respectively. Although the curve shapes are similar, the magnitude of the maximum particle-wall interaction (about 70 k_BT when 1 mM) is about twice the maximum particle-particle interaction (about 35 k_BT when 1 mM). At 1 mM, the particle-particle DLVO interaction shows a repulsive curve with a potential barrier of about 35 k_BT. At 10 mM, the curve shows a weaker repulsive interaction with a secondary minimum of about -0.7 k_BT and a potential barrier of about 10 k_BT. At 100 mM, it shows an attractive interaction with only the primary minimum. That is, in the case of 1 mM, the particles exist as a primary particle and are well dispersed due to the electrostatic repulsion. However, as the concentration of NaCl increases, the agglomerates are formed due to the screening of the electrostatic repulsion (see **Fig. 2.3a-c**).

2.3.2. Effect of salt concentration on particle deposition

Fig. 2.5 shows the particle deposition behavior according to the NaCl concentration at a flow rate of 1.2 ml/hr. For clarity, the boundary of the channel wall is marked with a blue line and the flow direction is indicated by a blue arrow. The upstream and downstream are defined as the upper and lower areas of approximately 300 pixels around the contraction, respectively.

The deposition pattern is dramatically different according to the salt concentration. In the case of 1 mM, the particles begin to deposit mainly in downstream, which turns black at 130 min due to the deposited particles. It should be noted that the color change of downstream to black does not mean that the channel is completely blocked. This behavior is consistent with the results of Kim *et al*.[41], where well-dispersed PS suspension with a negative surface charge was used. When the salt concentration is 100 mM, however, most particles are deposited in upstream and few particles are deposited in downstream. The deposition behavior of 10 mM is similar to that of 100 mM, but more particles are accumulated in the downstream than that of 100 mM. This tendency is observed too under flow rates of 0.3 ml/hr and 0.7 ml/hr (**Fig. 2.6**).

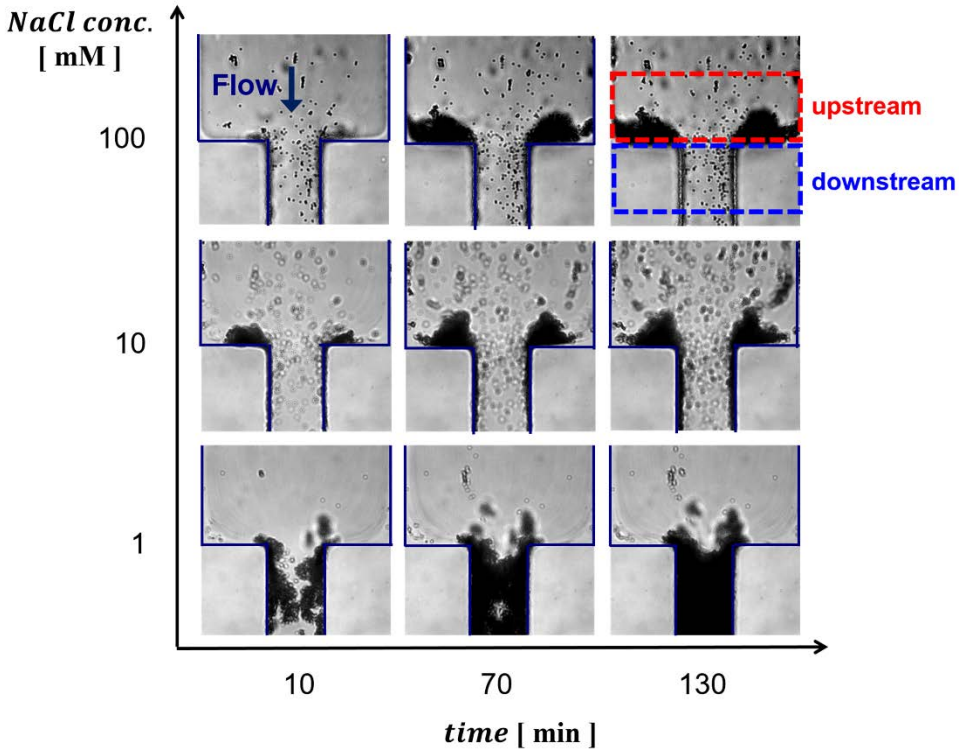

Fig. 2.5. Effect of salt concentration on particle deposition when q = 1.2 ml/hr. Flow direction is from top to bottom as indicated by the blue arrow.

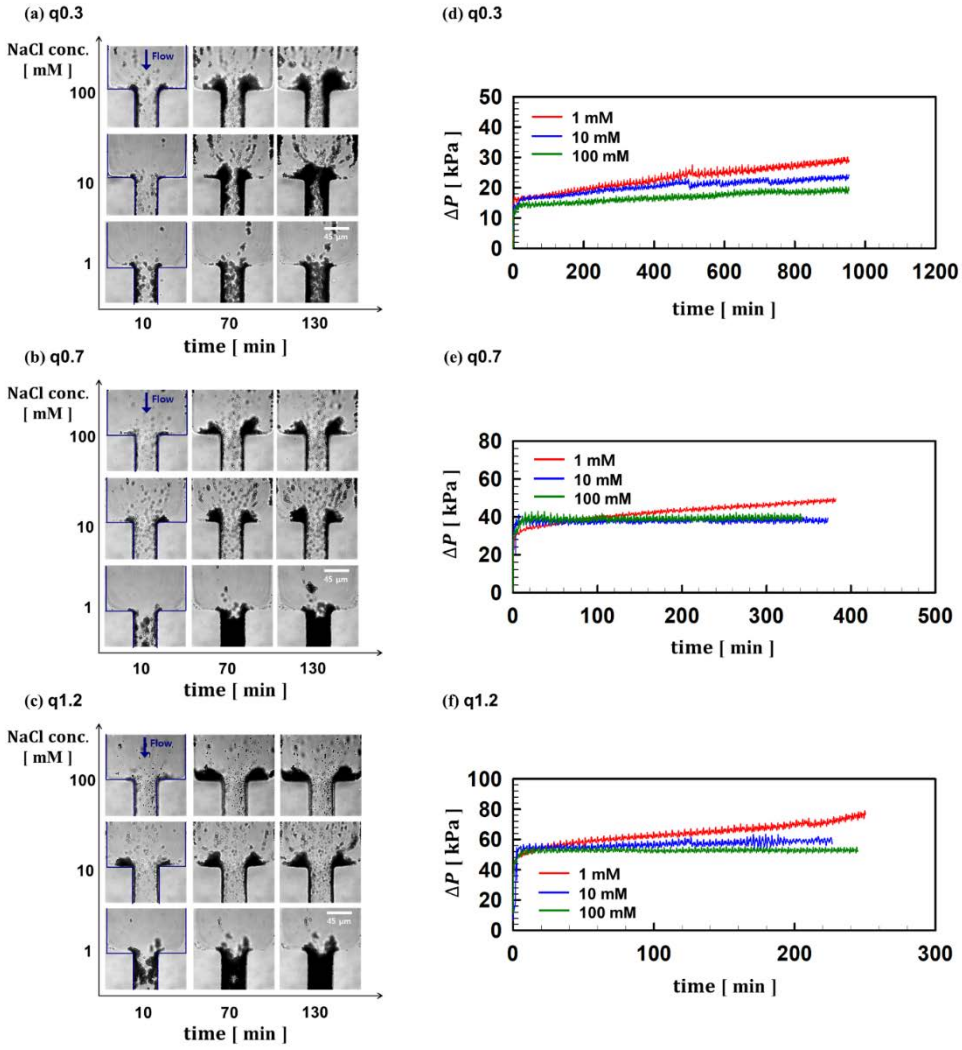

Fig. 2.6. Effect of salt concentration on particle deposition: (a) q0.3, (b) q0.7, and (c) q1.2, and the effect of salt concentration on pressure drop: (d) q0.3, (e) q0.7, and (f) q1.2.

Fig. 2.7 shows the image processing technique to quantify the number of particles deposited upstream and downstream. As mentioned in **Fig. 2.5**, image processing is performed by setting the upstream and downstream area as the 300 pixels above and below the contraction line. That is, the observation window is an area that corresponds to the width of 180 μm (1000 pixels) and the height of 108 μm (600 pixels). After converting the raw images into black-and-white binary images, the number of black pixels in the upstream and downstream is counted over time. Here, the number of black pixels is defined as the particle deposition area (A_d). **Fig. 2.7b**, **2.7c**, and **2.7d** illustrate the particle deposition area (A_d) corresponding to each salt concentration under q1.2 condition. In **Fig. 2.7b**, A_d of the downstream increases more rapidly than that of the upstream, which coincides with **Fig. 2.5**. On the other hand, in **Fig. 2.7c** and **2.7d**, A_d of the upstream increases faster than that of the downstream as the salt concentration increases from 10 mM to 100 mM. This result is consistent with the tendency of the particles that accumulate mainly in upstream, as can be seen in **Fig. 2.5**. Significant fluctuations of A_d are observed in **Fig. 2.7d**, as the accumulated clogs are broken up by the flow while the particles keep on accumulating. As the salt concentration increases, A_d of the upstream increases and A_d of the downstream decreases.

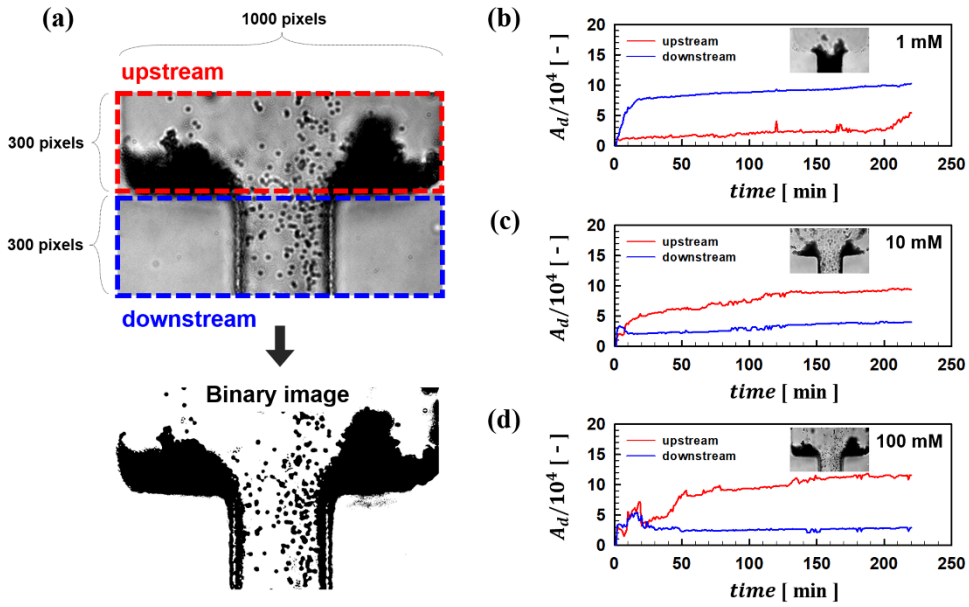

Fig. 2.7. (a) The upstream and downstream domain of the microchannel, marked with red and blue boxes, respectively. The original image, taken by the CCD camera, was converted to a black-and-white binary image. The particle deposition area (A_d), defined as the number of black pixels in each domain, was evaluated at (b) 1 mM, (c) 10 mM, and (d) 100 mM, as a function of time. The flow rate was fixed at q1.2 and the inset images were taken at 160 min.

So far, the differences in deposition behavior are confirmed through the images taken by the CCD camera and the calculated particle deposition area (A_d). However, the CCD image, which is two-dimensional, cannot reflect three-dimensional flow characteristics. In addition to 2D visualization, the pressure drop across the microchannel is measured as a complementary tool. The pressure drop without particles at different flow rates is provided in **Fig. 2.8**.

Fig. 2.9 shows the pressure drop at each salt concentration under the conditions of q1.2. In the case of 1 mM, where deposition occurs only in downstream, the pressure drop gradually increases from 50 kPa to 70 kPa. The reason for this increase in pressure drop can be explained by the Hagen-Poiseuille law. For the simple square duct flow at constant flow rate (Q), the pressure drop (ΔP) is inversely proportional to the square of the cross-sectional area (A_c) of the duct ($\Delta P = 8\pi\eta LQ/{A_c}^2$, where L is the channel length). In other words, 1.4 times increase in pressure drop from 50 kPa to 70 kPa means that the cross-sectional area of the channel is decreased by a factor of $\sqrt{1.4}$. As the successive particle deposition reduces the cross-sectional area where the fluid can flow, the pressure drop increases. For example, the values for 1 mM q0.3 condition is compared. The pressure drop changed from 15 kPa (at t=0 min) to 21 kPa (at t=130 min), and the cross-sectional area of downstream changed from 4,500 μm^2 to 3,600 μm^2. The cross-sectional area was obtained with the assumption that uniform deposition occurred to the thickness direction. The root of the pressure drop ratio was 1.18, and the ratio of the cross-sectional area inverse was 1.25. The results are comparable to each other. The cause of the error may lie in the assumption (uniform deposition) used in calculating the area. On the other hand, when the salt concentration is 100 mM, the pressure drop maintains the initial value of 50 kPa and significant changes are not observed. At 100 mM, the deposition occurs only in

upstream, and no deposition occurs in downstream (see **Fig. 2.5**). In the contraction channel, as most of the pressure drop is generated in downstream with a small cross-sectional area, there is little change in pressure drop when the particle deposition is reduced in downstream. The changes in pressure drop according to the salt concentration show a similar trend for the flow rates of q0.3 and q0.7 (**Fig. 2.6**). The pressure drop gradually increases when the deposition occurs downstream.

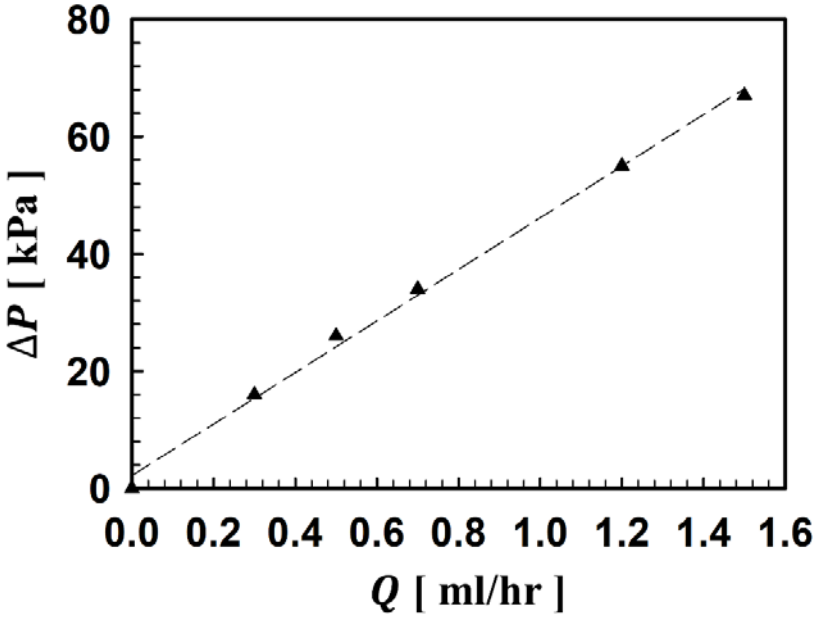

Fig. 2.8. The pressure drop without PS particles at different flow rates.

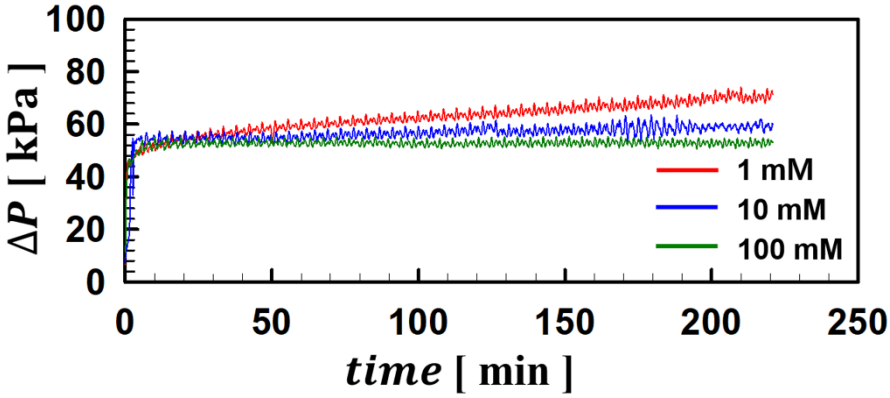

Fig. 2.9. Pressure drop as a function of time for q = 1.2 ml/hr.

2.3.3. Effect of flow rate on particle deposition

To observe the effect of flow rate on the particle deposition, the samples with various salt concentrations are injected into the contraction channel under three flow rate conditions. **Fig. 2.10** shows the overall pattern and the pressure drop. Additional replicated results are presented in **Fig. 2.11**. At 1 mM, the particle deposition occurs in downstream for all flow rate conditions and it becomes faster as the flow rate increases (**Fig. 2.10a**). At 100 mM, the deposition is observed both in downstream and upstream at q0.3 (**Fig. 2.10b**). The number of particles accumulated in downstream decreases sharply as the flow rate increases which leads the particles to accumulate only in upstream at q1.2.

The progress of particle deposition is closely related with the development of pressure drop (**Fig. 2.10c** and **2.10d**). At 1 mM, the pressure drop gradually increases with time at all flow rate conditions, as the particles are deposited in downstream, which leads to the reduction in cross-sectional area (**Fig. 2.10c**). That is, if particle deposition proceeds rapidly, the cross-sectional area also decreases rapidly, which leads to a sharp increase in pressure drop. In this way, the progress of particle deposition can be indirectly confirmed by the change in pressure drop over time. The slope of pressure drop with time increases as the flow rate increases. At 100 mM, the pressure drop gradually increases since some particles accumulate in downstream at q0.3. The slope of pressure drop is smaller than that of 1 mM q0.3 (**Fig. 2.10d**). For q0.7 and q1.2, since the particles are mainly deposited in upstream, the cross-sectional area of the channel does not decrease and no significant change in pressure drop is observed. The trend of 10 mM sample is similar to that of 100 mM which is presented in **Fig. 2.12**. The origin of regular fluctuation of the pressure drop seems to be a

mechanical pulsation of the pump.

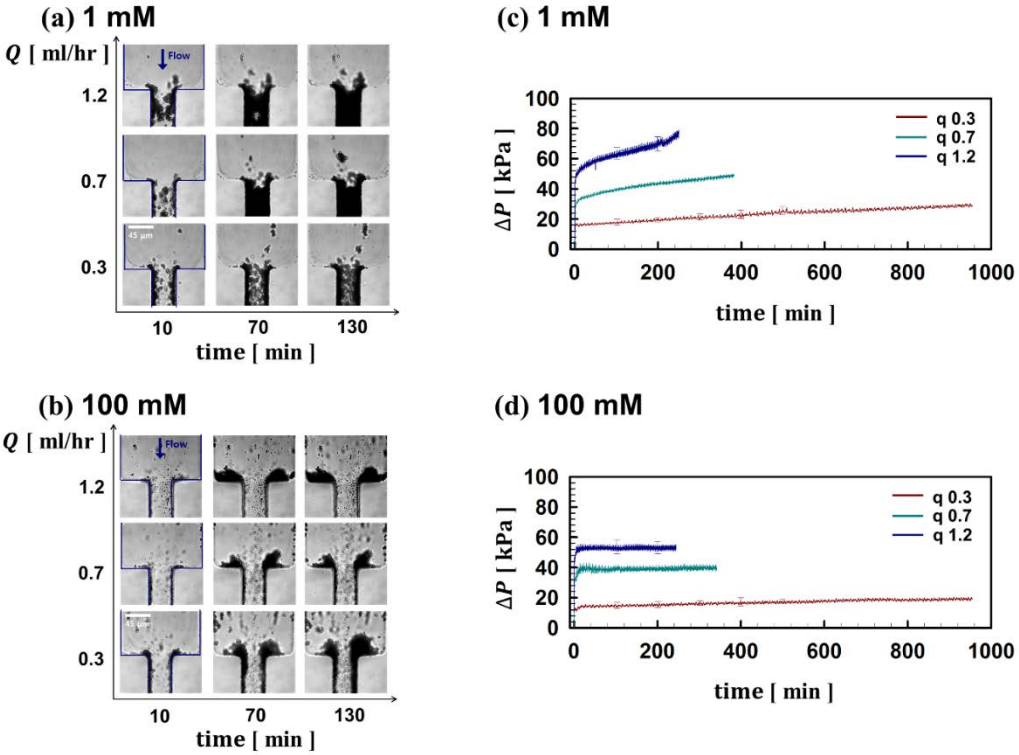

Fig. 2.10. Effect of flow rate on particle deposition: (a) 1 mM and (b) 100 mM, and on pressure drop: (c) 1 mM and (d) 100 mM. The error bars are displayed at some points (per every 100 min for q0.3 and q1.2).

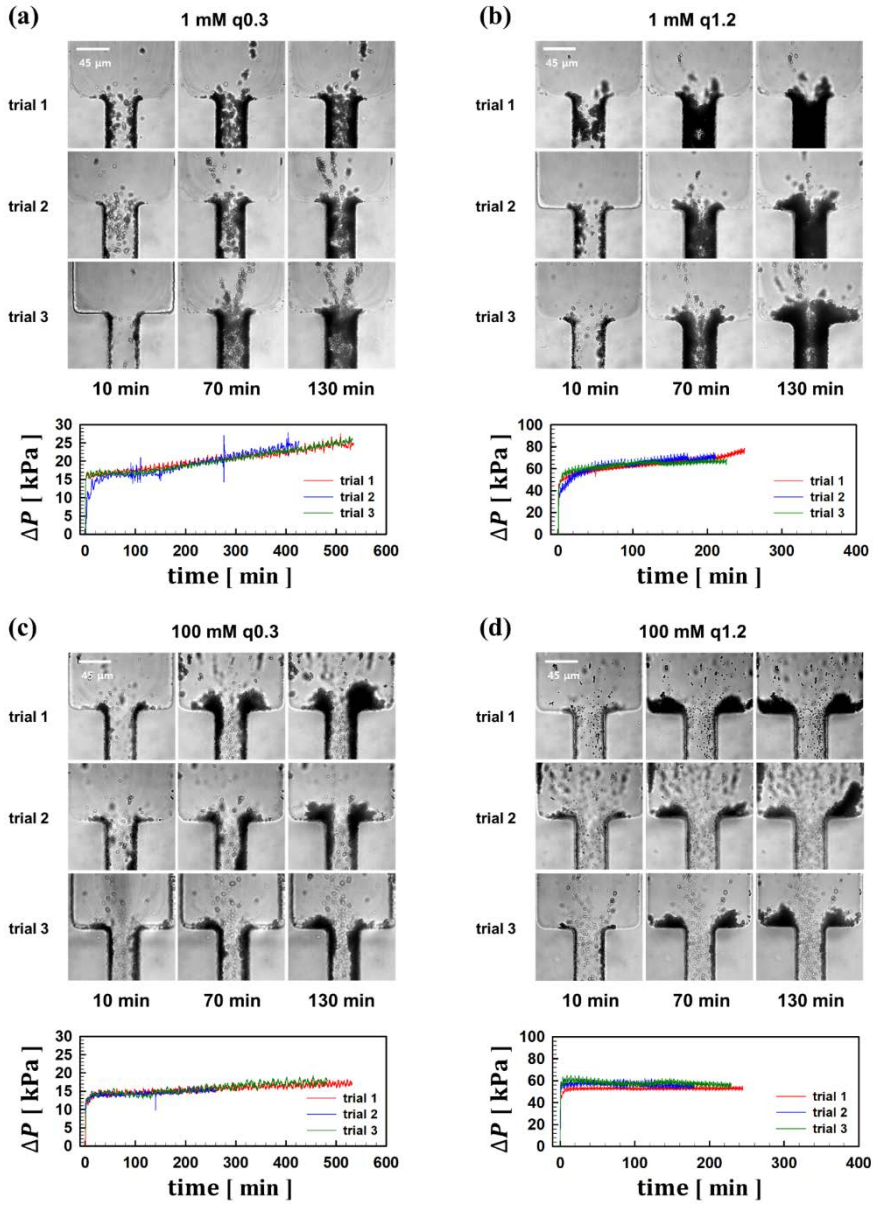

Fig. 2.11. Additional replicated results of 1 mM and 100 mM samples under each flow rates: (a) 1 mM q0.3, (b) 1 mM q1.2, (c) 100 mM q0.3, and (d) 100 mM q1.2.

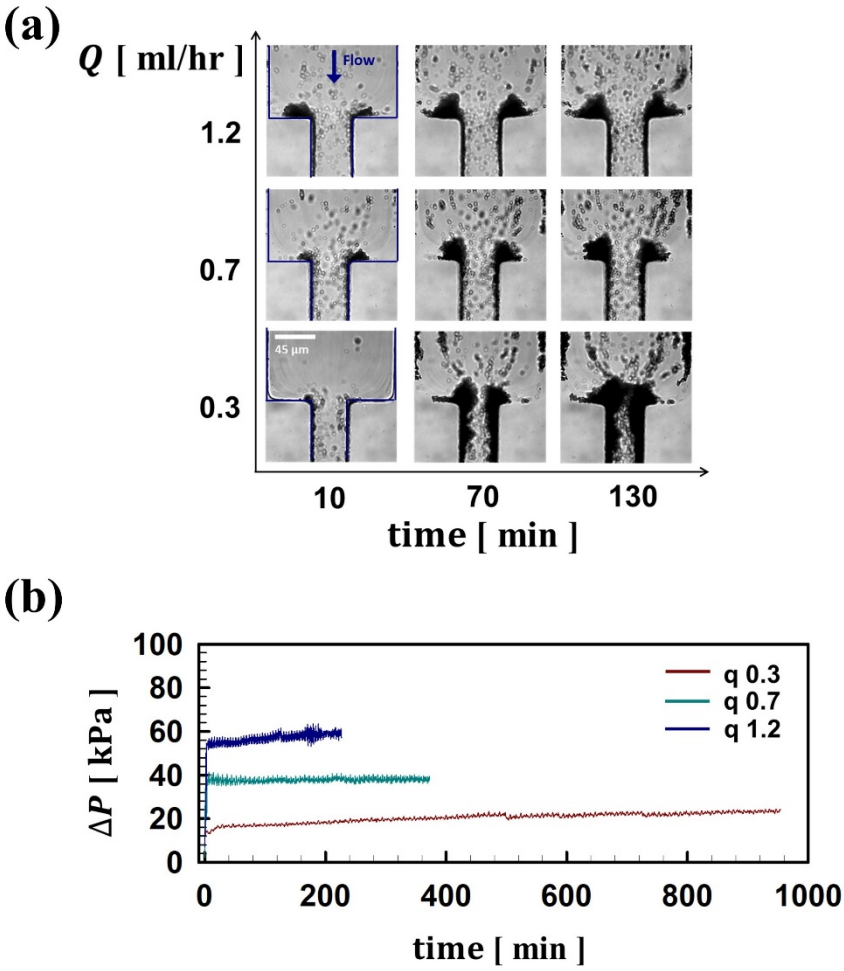

Fig. 2.12. Effect of flow rate on (a) particle deposition and (b) pressure drop at 10 mM.

Fig. 2.13 shows the particle deposition area (A_d) obtained from the images of 1 mM and 100 mM samples in **Fig. 2.10**. The deposition behaviors of 1 mM and 100 mM samples are significantly different at all flow rate conditions. At 1 mM, A_d of downstream (blue line) is larger than that of upstream, whereas at 100 mM, A_d of upstream (red line) is larger than that of downstream. At 1 mM, the deposition rate in downstream increases as the flow rate increases (see **Fig. 2.10c**). A_d of downstream quickly increases and saturates after a certain period of time. The saturation time becomes shorter as the flow rate increases (**Fig. 2.13a-c**). In particular, when the flow is given for a long time, more and more particles are accumulated in downstream. Eventually, at 1 mM q0.3, the deposition is extended to the upstream after 400 min resulting in a late increment of A_d of upstream (see inset of **Fig. 2.13a**). This clogging process is consistent with the results of Kim *et al*.[41]. At 100 mM, the particle deposition occurs in upstream at all flow rate conditions, and the number of particles accumulated in downstream decreases as the flow rate increases. When comparing the A_d of the downstream at 200 min, A_d decreases as the flow rate increases, where the inset image reflects the A_d graph (see inset of **Fig. 2.13d-f**).

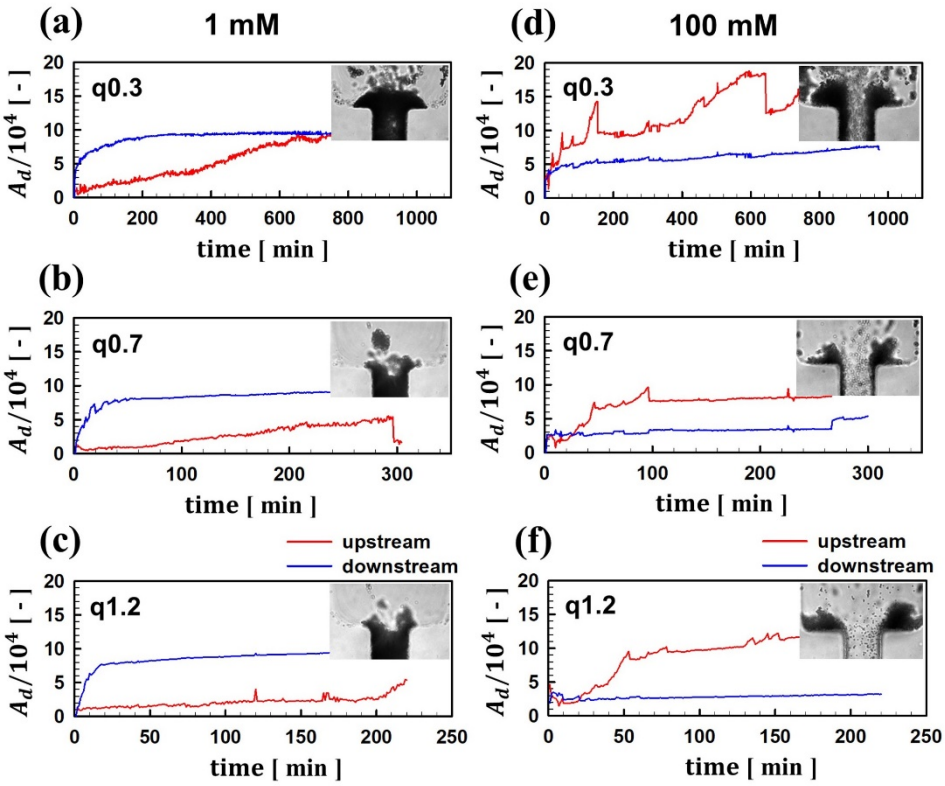

Fig. 2.13. Particle deposition area (A_d) of 1 mM and 100 mM samples at each flow rate. The inset images are snapshots at 800 min (q0.3), 200 min (q0.7), and 150 min (q1.2): (a) 1 mM, q0.3, (b) 1 mM, q0.7, (c) 1 mM, q1.2, (d) 100 mM, q0.3, (e) 100 mM, q0.7, and (f) 100 mM, q1.2.

2.3.4. Flow simulation

To characterize the flow inside the channel, two-dimensional numerical simulation is performed using a commercial computational fluid dynamics (CFD) software, COMSOL Multiphysics 4.2 (COMSOL Inc., USA). Since the working fluid has a constant viscosity independent of shear rate ($\dot{\gamma}$) (**Fig. 2.1**), the Navier-Stokes equation and the continuity equation are solved assuming the laminar flow of an incompressible Newtonian fluid.

$$\rho(\boldsymbol{u} \cdot \nabla \boldsymbol{u}) = -\nabla P + \eta \nabla^2 \boldsymbol{u} \tag{7}$$

$$\nabla \cdot \boldsymbol{u} = 0 \tag{8}$$

where ρ is the fluid density, $\boldsymbol{u}$ the fluid velocity, and P the pressure. A constant volumetric flux is assumed at channel inlet ($Q = Q_{in}$), no-slip boundary condition ($\boldsymbol{u} = \boldsymbol{0}$) is applied at wall, and $P = 0$ is assumed at outlet. The number of elements used in the simulation is 21,281. The wall shear stress (σ_{wall}) is calculated as the product of the shear viscosity (η) and the wall shear rate ($\dot{\gamma}_{wall}$) at each flow rate ($\sigma_{wall} = \eta \dot{\gamma}_{wall}$).

Fig. 2.14a and **Fig. 2.14b** depict the contour of the flow velocity and the hydrodynamic stress at each flow rate. The velocity increases as it moves from upstream to downstream, and the wall shear stress in downstream is larger than that in upstream. **Fig. 2.14c** shows the wall shear stress in upstream and downstream at different flow rates. The upstream stress is calculated as the average wall shear stress on the wall indicated by the red solid line in the inset image, while the downstream stress is calculated as the average on the wall indicated by the blue dotted line. At all

flow rates, the downstream wall shear stress is at least 40 times larger than the stress in upstream. In addition, both upstream and downstream wall shear stress increases with the flow rate.

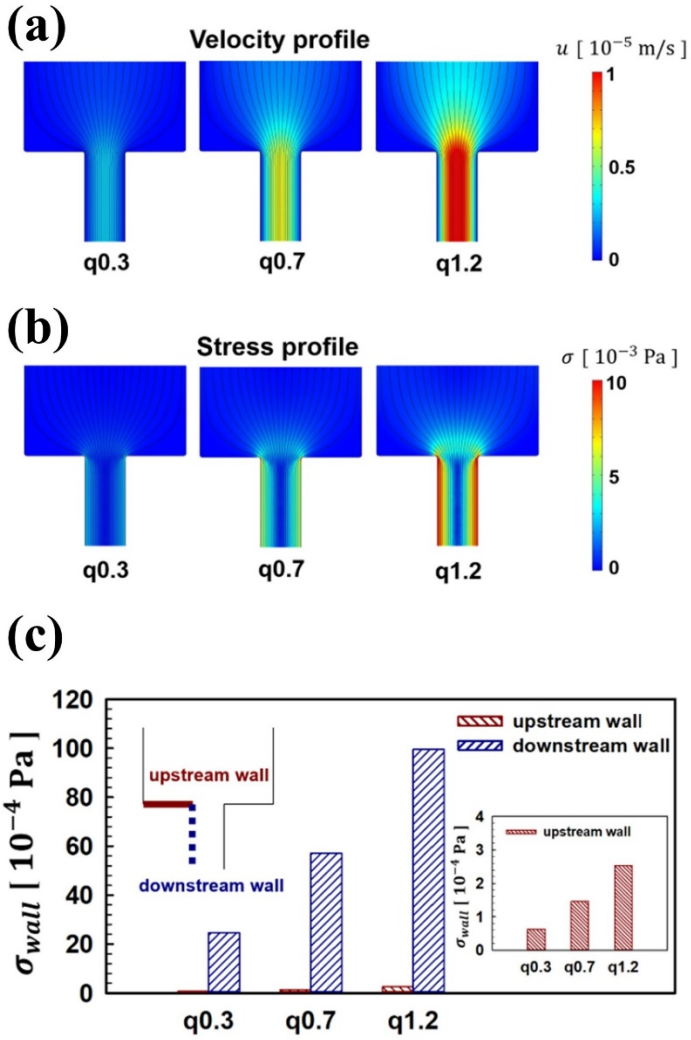

Fig. 2.14. (a) Velocity and (b) stress profile of q0.3, q0.7, and q1.2. (c) Wall shear stress in upstream and downstream for different flow rates. Wall shear stress in upstream is provided in the inset. Upstream and downstream walls are distinguished by color.

2.3.5. Clogging dynamics

Until Section 2.3.4, particle deposition behaviors in both upstream and downstream part of the microchannel were examined according to the salt concentration and flow rate. In addition, the wall shear stress of the channel was calculated by flow simulation. As the wall shear stress plays a role that pushes the particle away from the wall and the downstream wall shear stress is at least 40 times larger than the upstream, it can be expected that the particle deposition in downstream would be significantly hindered by high wall shear stress. However, at 1 mM (see **Fig. 2.10a**), most of the particle deposition occurs in downstream while almost no particle deposition is identified in upstream. At 100 mM, on the other hand, the opposite behavior is observed. Particle deposition hardly occurs in downstream, whereas the deposition occurs mostly in upstream (see **Fig. 2.10b**). It is difficult to explain the observed behavior in terms of the wall shear stress alone, and other forces must be considered as well.

To investigate the reason for the difference in particle deposition behavior when the salt concentration changes, the forces acting perpendicular to the wall need to be considered. When sedimentation and diffusion are neglected, the forces acting on charged spherical particles passing through the proximity of a flat surface in laminar shear flow are the lift force and colloidal force [45]. The particle-wall colloidal force (F_C) at a distance of 0.1R away from the wall is calculated by Eq. (9).

$$F_C = -\left.\frac{dU_{total,p-w}}{dh_2}\right|_{h_2=0.1R} \tag{9}$$

where $U_{total,p-w}$ is the particle-wall DVLO interaction potential and h_2 is the surface-to-surface distance between the particle and the wall.

The lift force (F_L) is a representative force that induces lateral migration by acting on a direction that repels the particle away from the wall [46]. The presence of a channel wall causes a velocity gradient to form within the fluid, resulting in varying velocities across different layers. This velocity gradient induces shear forces between adjacent fluid layers. Consequently, if a particle is present within the fluid, it will start to spin due to the influence of these shear forces. Additionally, the particle experiences an extra drag force that causes it to move in the opposite direction of the fluid flow. This phenomenon, known as slip shear, generates a lateral force on the particle, ultimately manifesting as a shear-gradient lift force. Saffman theoretically determined the lift force and it is estimated as follows.

$$F_L = 6.46\rho\eta^{0.5}\dot{\gamma}^{0.5}D^2V \tag{10}$$

where ρ is the fluid density, $\dot{\gamma}$ the shear rate, D the particle diameter, and V the relative velocity between the particle and the fluid. The lift force is proportional to the square root of the wall shear stress and the square of the particle diameter.

At a distance of 0.1R, DLVO potential clearly differentiates the repulsive force and the attractive force. If the distance is closer than the location of energy barrier, all the curves fall into a primary minimum, while the force ratio between lift force and colloidal force does not change much when it is larger than 0.1R. Thus, all forces are calculated at a distance of 0.1R

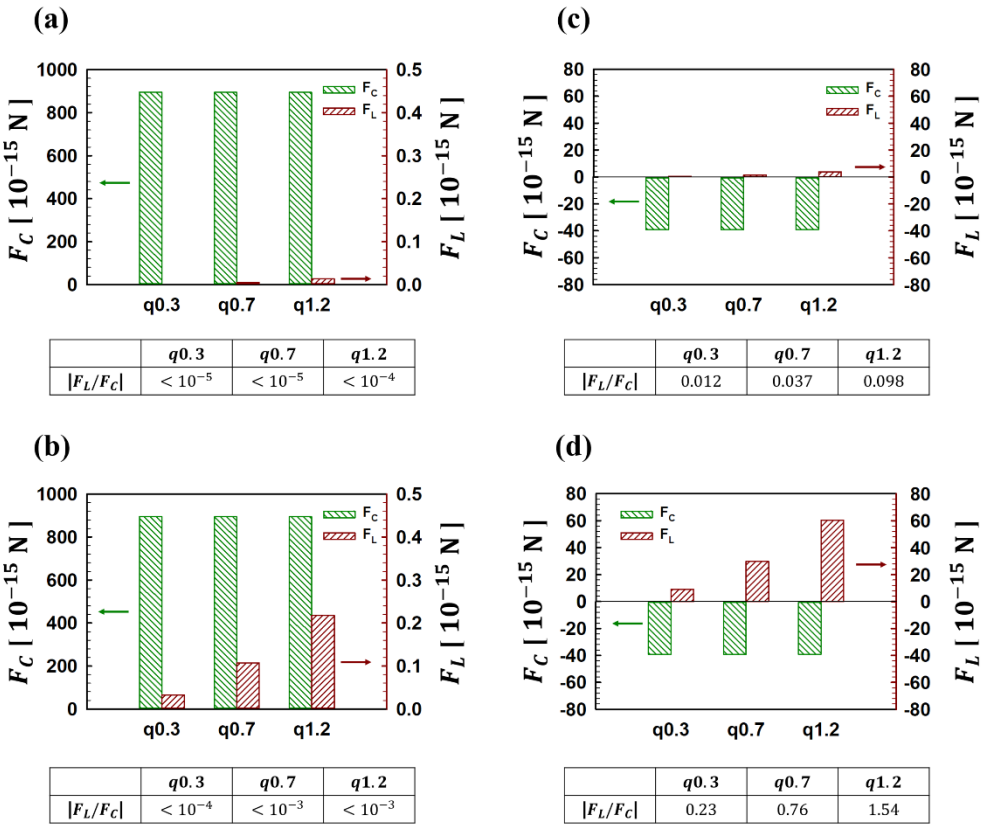

Fig. 2.15. Colloidal force (F_C) and lift force (F_L) acting on the particle in the proximity of upstream and downstream wall at each flow rate condition: (a) 1 mM upstream, (b) 1 mM downstream, (c) 100 mM upstream, and (d) 100 mM downstream. The table shows the ratio of lift force to colloidal force.

Fig. 2.15 shows the colloidal force and lift force acting on the particle adjacent to the upstream and downstream wall. When the salt concentration is 1 mM (**Fig. 2.15a** and **2.15b**), as the colloidal force is positive (which means repulsive), it repels the particle from the wall, as the lift force does. On the other hand, when the salt concentration is 100 mM (**Fig. 2.15c** and **2.15d**), the colloidal force is negative (which means attractive), acting in the opposite direction to the lift force, which makes the particle move to the wall. In addition, the lift force of the 100 mM sample is larger than that of 1 mM sample. This is because the particle is bigger for 100 mM due to the formation of particle agglomerates as shown in **Fig. 2.3** (see Eq. (10)).

Fig. 2.15a shows the forces acting in the upstream when the salt concentration is 1 mM. The colloidal force is much larger than the lift force, and both forces act in the same direction, repelling the particles away from the wall. **Fig. 2.15b** shows the forces acting in the downstream when the salt concentration is 1 mM. Though the lift force is increased and the repulsive colloidal force is present, particle deposition occurs mostly in downstream (see **Fig. 2.10a**). Since the particles still deposit in downstream despite the back transport by the colloidal force and lift force, it can be inferred that there should be another particle transport mechanism to the wall. In previous studies, the concept of 'particle flux density' was introduced to explain the particle deposition in contraction geometry [47, 48]. When the suspension flows from the upstream to downstream, the particle flux flowing through the cross-sectional area of the channel increases rapidly due to the sudden contraction. This can lead to temporary jamming of the particles, which develops into pore clogging [47, 48]. This explanation is also valid in our observation. The particle deposition accelerates as the flow rate increases in **Fig. 2.10a**, which can be explained by the increment of the particle flux density. An increased flow rate leads to an increment of particle flux

density, finally leading to faster particle deposition rates.

Fig. 2.15c shows the forces acting in the upstream at 100 mM. In this condition, an attractive colloidal force acts and the lift force increases as the colloidal size increases. The direction of the two forces are opposite and the attractive colloidal force is at least 10 times larger ($|F_L/F_C| = 0.098$ at q1.2), up to even 100 times ($|F_L/F_C| = 0.012$ at q0.3) than the lift force, which leads the attractive colloidal force to become significant. The particle deposition in upstream (see **Fig. 2.10b**) can be explained by the attractive particle-wall interaction. **Fig. 2.15d** shows the forces acting in downstream at 100 mM. Like the 1 mM sample, the particle flux density increases in downstream. At 100 mM, however, the lift force increases due to the increase in wall shear stress, which is almost comparable to the colloidal force. As the flow rate increases, the lift force increases and becomes about 1.54 times larger than the colloidal force at q1.2 ($|F_L/F_C| = 1.54$ at q1.2). The increased lift force due to fast flow rate will inhibit particle deposition. This matches with particle deposition in downstream, which decreases with the increase in flow rate, and almost no particle is deposited at q1.2 (see **Fig. 2.10b**).

To summarize the discussions so far, in the upstream, as the colloidal force is more dominant than the lift force, the particle deposition occurs when the interaction is attractive and it does not occur when the colloidal interaction is repulsive. Meanwhile, in the downstream, the particle flux density increases due to sudden contraction, so that the particle deposition is more likely to happen in downstream than in upstream. However, when the particle agglomerates are formed due to attractive colloidal force, the lift force increases and leads to less particle deposition in downstream. If the lift force affects the clogging dynamics as shown in the experiments, it can be inferred that the particle deposition will show a different pattern if the colloidal size is changed

even though the colloidal interaction is similar. In this regard, an experiment set is designed to investigate the change in the deposition behavior in downstream when the colloidal size is controlled through sonication.

2.3.6. Effect of agglomerate size on particle deposition

Fig. 2.16a shows the change in agglomerates size over time when the agglomerates are broken up by applying sonication and placed in a rest state. Both 1 mM and 100 mM are sonicated for 20 minutes to break up all the existing agglomerates where the size change is monitored with time. There is no difference in dispersion state before and after sonication when the salt concentration is 1 mM. However, the 100 mM sample shows a clear difference in dispersion state. After sonication, all the agglomerates are broken up into primary particles, and the agglomerates are gradually regenerated as time proceeds. When 24 hours have passed after sonication, some agglomerates are re-formed. **Fig. 2.16b** shows the change in Feret diameter (d_F) with time when the salt concentration is 100 mM. The size of more than 150 agglomerates is measured. The diameter and its deviation hardly change until 240 minutes after sonication and then slightly increases thereafter. It means that the effect of particle aggregation due to flow can be negligible because the time scale for particles to pass through the channel is much shorter that the time scale for particles to form agglomerates, if the experiments are performed within 4 hours.

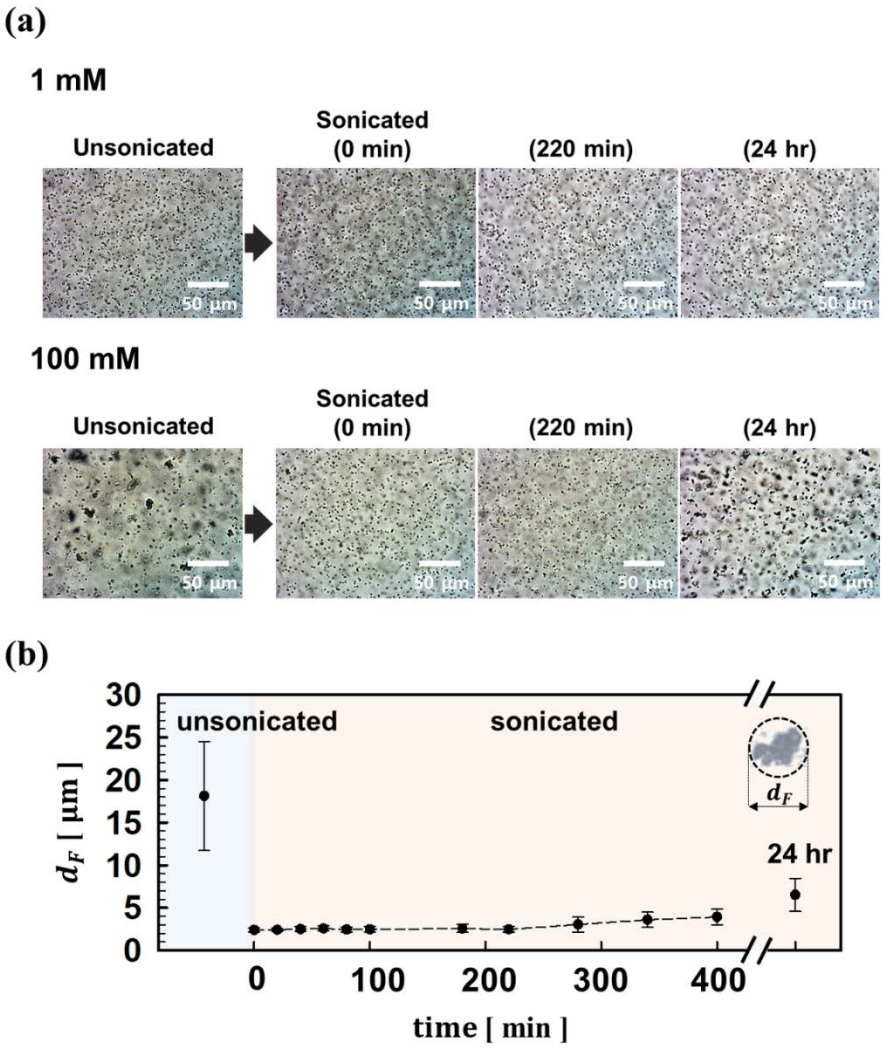

Fig. 2.16. (a) The microscope images of 1mM and 100 mM sample before and after sonication. (b) Size recovery of 100 mM sample over time after sonication. The size measured is the Feret diameter (d_F).

Fig. 2.17 shows the particle deposition behavior at q0.3 and q1.2 for 100 mM samples with and without sonication. Since all flow tests are conducted within 4 hours, the effect of flow-induced particle aggregation is negligible. All flow tests are performed at least 3 times, and show consistent results. In **Fig. 2.17a** and **2.17b**, the deposition behavior of unsonicated and sonicated samples are almost the same except for fluctuation caused by the breakup of clogs, and it is difficult to find a significant difference. Because $|F_L/F_c| = 0.23$ at q0.3 is not large (see **Fig. 2.15d**), the change in lift force according to the colloidal size reduction due to sonication does not have a significant effect on particle transport. On the other hand, at q1.2 in **Fig. 2.17c**, there is a noticeable difference in particle deposition depending on sonication. In the unsonicated sample where agglomerates are present, almost no deposition occurs in downstream. For the sonicated sample where the agglomerates are broken up, the deposition in downstream increases significantly. When the colloidal size is reduced by sonication, the lift force is reduced as well and the change in lift force has a significant effect on particle transport because of $|F_L/F_c| = 1.54$ at q1.2 (see **Fig. 2.15d**). In **Fig. 2.17d**, the downstream deposition area of the sonicated sample increases significantly compared to that of the unsonicated sample. Compared to 130 min, when the particle deposition in downstream is almost steady, the downstream deposition area of the sonicated sample is increased by about 86% from the unsonicated sample. Therefore, in the case of unsonicated sample, larger colloidal size results in larger lift force, which leads to less deposition in downstream. The cause of downstream particle deposition in the sonicated sample seems to be a decrease in lift force due to a reduction in colloidal size.

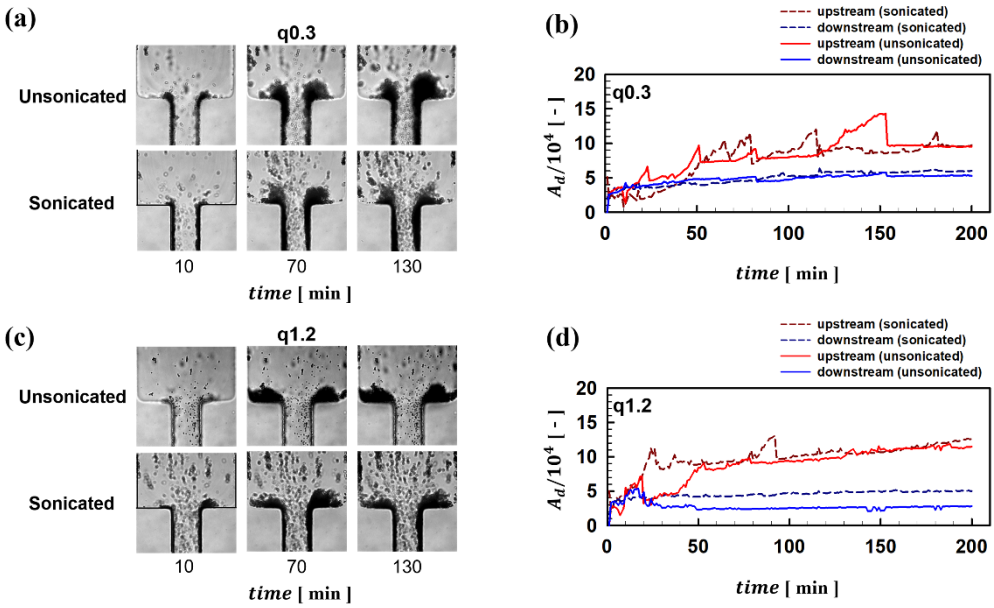

Fig. 2.17. Comparison of unsonicated and sonicated samples (100 mM) at (a) q0.3 and (c) q1.2. Particle deposition area (A_d) at (b) q0.3 and (d) q1.2.

2.4. Conclusions

In this chapter, the clogging dynamics in the contraction microchannel and its mechanism were investigated by considering the forces acting on the particles. The single-pore clogging process was observed through a flow visualization setup using microfluidics, and the flow characteristics inside the channel were calculated through CFD simulation and then correlated with the observed results. Significant differences in particle deposition characteristics were observed. When the salt concentration was 1 mM and the particle interaction was repulsive, the particle deposition occurred only in downstream and rarely in upstream at all flow rate conditions. On the contrary, when the salt concentration was 100 mM and the particle interaction was attractive, the deposition behavior was opposite to that of 1 mM. When the flow rate was low, the particle deposition occurred both in upstream and downstream. At high flow rates, the particle deposition occurred only in upstream.

The difference in particle deposition behavior according to salt concentration and flow rate was explained by the particle flux density and the ratio of lift force to colloidal force. For 1 mM sample with repulsive interaction, both colloidal and lift forces acted to repel the particles away from the wall and the particle deposition was inhibited in upstream. However, in downstream, the particle deposition occurred in spite of the increased repulsive force, which was explained by the increased particle flux density in downstream. For the 100mM sample with attractive interaction, the particle deposition characteristics were explained as follows. In the upstream, the particle deposition occurred because the attractive colloidal force was larger than the lift force at all flow rate conditions. However, as the flow rate increased in downstream, the lift force increased and the particle deposition decreased. Meanwhile,

sonication was applied to the prepared sample to analyze the effect of colloidal size on particle deposition. When the agglomerates of the 100 mM sample were broken up by sonication, the colloidal size decreased and the lift force also decreased, resulting in the increased particle deposition in downstream.

This study helps to elucidate the specific behavior and the mechanism of particle deposition in a single-pore as a fundamental study of membrane fouling and pore clogging because the clogging mechanism is comprehensively identified from the colloidal interaction and hydrodynamics stress. The results of this study show that the location where the deposition occurs in the pore can be controlled to some extent by changing the colloidal interaction and flow conditions, suggesting the possibility of alleviating clogging issues through deposition control. Ultimately, a comprehensive understanding of clogging dynamics with the colloidal interaction and hydrodynamics would lead to a systematic approach to prevent clogging that occurs at severe contraction like jetting nozzles or pipe orifices.

Chapter 3.

Particle deposition and clogging in the cross-flow through a T-shaped microchannel

3.1. Introduction

Membrane filtration is a widely used unit process that is essential in various industrial fields. In particular, membrane filtration is used intensively for semiconductor CMP slurries [49-51], battery slurries [52, 53], waste-water treatment [54-57], food industry [58, 59], and pharmaceutical and biological fractionation [60]. This filtration contributes to improving the quality by removing impurities from the particulate suspension and enhancing the homogeneity of the suspension. However, such filtration is often faced with membrane fouling or clogging issues due to continuous particle transport which leads to a degradation of the process performance and large losses in productivity. That is, membrane fouling and clogging are very undesirable phenomena and must be resolved to maintain the membrane function. To maintain the performance and function, various cleaning strategies such as back pulsing and back flow reversal have been introduced [61, 62]. However, these strategies are only temporary solutions to fouling and clogging, and it is necessary to identify the underlying clogging mechanism to prevent undesirable phenomena.

To identify the complicated clogging mechanism, microfluidics that facilitate the visualization of the clogging process have been extensively used in previous studies. In addition, microfluidics facilitates the control of geometrical parameters and flow conditions. The clogging mechanism of the microfluidic channel flow is classified as

sieving due to size exclusion [9], bridging or arching due to multiple particles reaching the pore at the same time [10], and aggregation induced clogging due to continuous particle deposition [11, 12]. In particular, aggregation induce clogging, which has been intensively studied recently, is determined by the interplay of the particle-wall, particle-particle colloidal interaction [12, 33, 63], and hydrodynamics [12, 34]. In addition, various factors such as the particle softness [64, 65], particle aggregates [36, 37], polydispersity [15, 31, 66], and geometric obstacles [32, 67] can affect the aggregation-induced clogging.

A membrane is a complex porous material composed of pores with various sizes. Filtration using these complex porous materials is classified into 2 types, which are dead-end flow and cross-end flow according to the direction of the pore and feed stream. The two methods can be characterized by the flow direction and the filtering direction. In the case of the dead-end flow, the directions of the flow and the filtering are parallel; however, in the cross-end flow, they are perpendicular. What is remarkable is that most of the preceding studies introduced above have been conducted with a focus on the dead-end flow. Compared to dead-end flow, cross-end flow has the advantages that the filter cake formed is relatively thin, and the flux decline is relatively small because the particles attached to the membrane can be washed away by the shear flow [68]. Despite these advantages, research on the cross-end flow is comparatively less studied. Song *et al*. [69] proposed a mathematical model to elucidate the underlying mechanisms of dynamic membrane fouling. The model was used to estimate the cross-membrane flux and time required to reach equilibrium fouling. Moreover, the authors used this model to optimize the performance of a crossflow filtration system. Chan *et al*. [70] analyzed the effect of pH and ionic strength on membrane fouling using a protein-containing solution. The

authors showed that the performance of a protein-separating membrane can be improved by controlling the protein-membrane interaction in the cross-flow. Recently, several studies were done to improve filtration performance by introducing the concept of hydrodynamic forces such as inertial force and centrifugal force into the cross-flow [71, 72]. Although these previous studies are valuable, they do not provide physical insight into the phenomena occurring in the pores inside the membrane. Meanwhile, Zwieten *et al*. [73] found that the rate of clogging was solely dependent on the trans-membrane flux. This was observed by controlling the flux through two outlets in a cross-flow system composed of multi-pores. It was discovered that an increase in the cross-membrane flux resulted in a slowing down of the particle deposition which in turn delayed the clogging. In addition, Agbangla *et al*. [48] studied the formation of filter cakes in the dead-end and cross-end flow systems with a focus on the effects of the particle concentration, flow rate, and salt concentration. The researchers observed that the filter cake had an unusual shape and pattern under the cross-end flow.

The contributions of Zwieten *et al*. [73] and Agbangla *et al*. [48] are significant because they provide valuable insights on the parameters that affect the phenomena occurring inside the pore. However, these studies remain phenomenological, as the variables analyzed in the studies are not directly related to the physical interaction between the particles and the wall. In the actual clogging process, the competing forces of attachment and detachment exerted on the particle play an important role. Therefore, to better understand the dynamics, it is necessary to quantify the effect of the flow conditions on the balance between the forces.

Specifically, the attachment force on the particle is originated from surface properties of particle such as the van der Waals interaction or hydrophobicity. The

detachment force is originated from hydrodynamic drag and it can be controlled mainly by the flow conditions, such as flow rate and medium viscosity. In particular, the hydrodynamic stress related to the detachment force that inhibits particle deposition can be an important parameter in determining the mechanism of clogging phenomena. Hydrodynamic stress is a typical variable that describes the flow, expressed as the product of viscosity and shear rate. Although the studies on the effect of hydrodynamic stress on clogging are necessary to provide a comprehensive understanding of flow characteristics, few studies have been conducted on the hydrodynamic stress, especially in the cross-flow. Additionally, there is a lack of studies on the effect of rheological properties, such as fluid viscosity, on the cross-flow clogging and particle deposition. This information is crucial to understand complex flows, which are not only induced by the flow channel but also by modified flow fields due to clogging and deposition.

In this study, the effect of hydrodynamic stress on the particle deposition and clogging in the cross-flow embodied by a T-shaped microchannel is investigated. To control the stress, the viscosity, a representative rheological property, is controlled by changing the glycerol concentration, while the flow rate is varied as well. Through this, we systematically investigate the particle deposition of a poly(styrene) particle suspension.

The paper is organized as follows. Section 2 presents the details of the experiments including fluids, microfluidic setup, and flow conditions. Section 3 provides the behavior of particle deposition and clogging. Image processing is conducted to quantify particle deposition and clogging. The blockage ratio and deposition ratio are introduced. The particle deposition is identified through a step-by-step process. In addition, the clogging is analyzed through the non-dimensional quantity calculated

by the hydrodynamic stress and the colloidal interaction. Section 4 summarizes the results and provides the concluding remarks.

3.2. Experimental

3.2.1. Materials

In this study, a well-dispersed suspension of polystyrene (PS) particles in an aqueous glycerol solution is used as the working fluid. Polystyrene (PS) latex (solid% = 4 %, surface charge density = 18.2 μC/cm^2, Invitrogen, USA) with a very high monodispersity of approximately 1.5(±0.05) μm in diameter is used, and the particle concentration in all sample is fixed at 0.1 wt%. The PS particle has a negative charge (ζ-potential ~ -32 mV, ζ-potential and particle size analyzer ELS-Z, Otsuka Electronics, Japan) due to the carboxyl group on the surface, so there is an electrostatic repulsion force which causes a high colloidal stability. Nevertheless, sonication is applied for more than 1 minute before each experiment to prevent any aggregation of particles that rarely occurs. To analyze the effect of the hydrodynamic stress on the particle deposition and the clogging, the medium viscosity of the working fluid is controlled. The viscosity is controlled by adjusting the concentration of glycerol, which can be set at 50%, 60%, 70%, or 80%. Although the permittivity of the medium or the zeta potential of the particles depends on the glycerol concentration, the change is negligible under the above concentration conditions, resulting in consistent particle-particle interactions. Glycerol is a typical Newtonian fluid whose viscosity remains constant regardless of shear rate. For the sample preparation, glycerol (Glycerin, Daejung Chemicals & Metals Co., Ltd., Korea) and deionized water are thoroughly mixed for 30 minutes. After that, the latex suspension subjected to sonication is added and mixed for 24 hours with a magnetic stirrer (180 rpm). The prepared samples are labelled as Gly50PS, Gly60PS, Gly70PS, and

Gly80PS according to the glycerol concentration.

Fig. 3.1 shows the flow curve of the prepared samples with and without PS particles. It can be confirmed that the samples of each concentration have constant viscosity independent of the shear rate. In particular, the addition of particles does not affect the viscosity of the glycerol solution. The viscosity of Gly50PS, Gly60PS, Gly70PS, and Gly80PS are 5.1, 8.9, 17.7, and 44.6 mPa·s, respectively, showing Newtonian behavior. The viscosity is measured by using a rotational rheometer, AR-G2 (TA instruments, USA) with 60 mm parallel plate at 25 ℃.

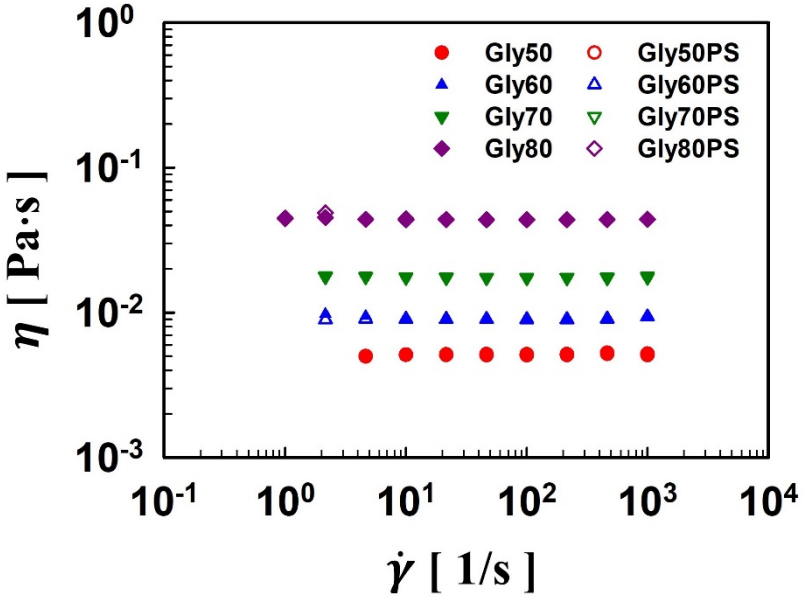

Fig. 3.1. Shear viscosity (η) of aqueous glycerol solution with and without PS particle. Addition of PS particle has no effect on shear viscosity of the samples.

3.2.2. Microfluidic setup

The experiment is performed in a T-shaped microchannel (**Fig. 3.2a**). The T-shaped microchannel consists of one inlet and two outlets. The fluid injected into the inlet exits through $\mathrm{Outlet}_{\perp}$ and $\mathrm{Outlet}_{\parallel}$, and there is no additional permeation at the outlet. All outlets are connected to the atmosphere. Height of the channel (H), trans-stream width of the channel ($W_{\perp}$), cross-stream width of the channel ($W_{\parallel}$) are 100, 50, and 100 μm, respectively, and the width ratio of the two outlets is 2:1. The channels are fabricated by using the SU-8 mold and poly(dimethyl siloxane) (PDMS, Sylgard 184A, Sewang Hitech Silicone, Korea). PDMS and curing agent (Sylgard 184B, Sewang Hitech Silicone, Korea) are mixed at a ratio of 10:1, poured onto a SU-8 mold with a channel design, and baked at 80 ℃ overnight. More detailed information on the fabrication process can be found in the cited paper [41]. The fabricated channel is transparent, so particle deposition and pore clogging behavior in the T-junction part can be observed. Inverted microscopy, IX-71 (Olympus, Japan) and highly sensitive CCD camera (Hamamatsu, Japan) are used to observe the particle deposition behavior (**Fig. 3.2b**). A syringe pump (PHD 4400, Harvard apparatus, USA) is used to inject the flow into the channel (**Fig. 3.2b**). Tygon tubing is used for all flow paths except the PDMS channel. Particle deposition images are taken at the T-junction with intervals of 1 minute through the observation setup in **Fig. 3.2b**.

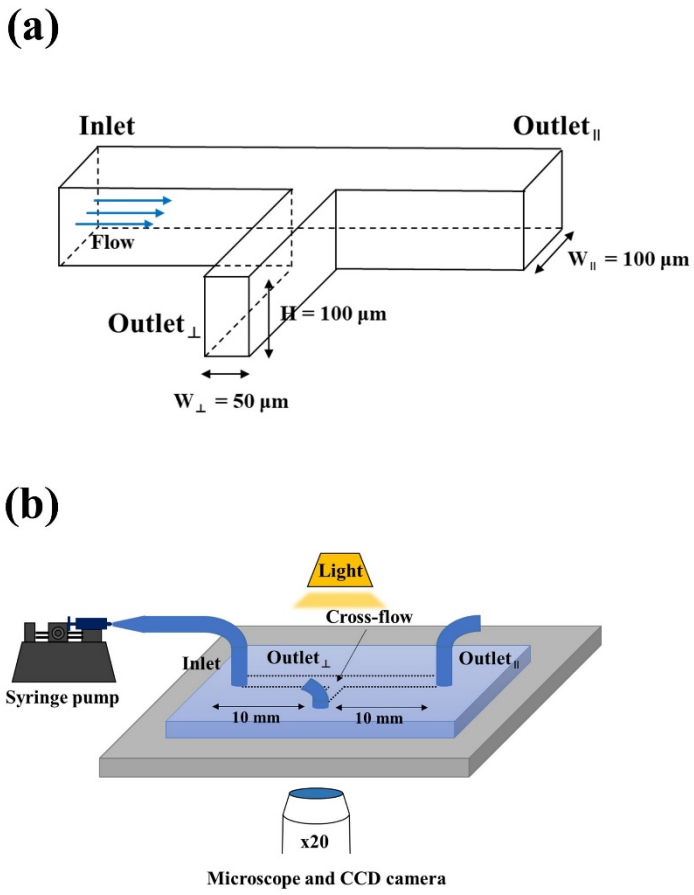

Fig. 3.2. (a) A projected view of the T-shaped microchannel ($W_{\perp}$: trans-stream width of the channel, $W_{\parallel}$: cross-stream width of the channel, H: height of the channel). Flow direction is indicated by blue arrows. (b) Schematic of the microfluidic observation system.

3.2.3. Flow conditions and hydrodynamics

Each sample is tested under five flow rate conditions of 0.7, 1.0, 1.2, 1.5, and 1.7 mL/hr. For convenience, flow rate conditions of 0.7, 1.0, 1.2, 1.5, and 1.7 mL/hr are labelled as q0.7, q1.0, q1.2, q1.5, and q1.7, respectively. As mentioned before, all flows are injected into the channel at a constant flow rate using syringe pump, and the images of particle deposition behavior at bifurcation region are recorded every minute through the CCD camera. The Injection volume of every experiment is fixed at 5 mL which is the maximum volume of syringe capacity. When the particle-free glycerol solution is injected, the volume flow rate ratio of the solution discharged through $\mathrm{Outlet}_{\parallel}$ to $\mathrm{Outlet}_{\perp}$ is approximately 5. **Table 3** shows the composition of the sample and the dimensionless number according to the flow rate conditions. Reynolds number (Re $= \rho \bar{V} D_h/\eta = 2\rho Q/(W_{||} + H)\eta$, the ratio of inertial force to viscous force, where ρ is the fluid density, $\bar{V} = Q/W_{||}H$ is the average velocity, Q is flow rate, D_h is the hydraulic diameter, and η is the shear viscosity.) corresponds to 0.05 – 1.04 at the flow rate used. Stokes number (St $= \rho_p d_p^2 \bar{V}/18\eta W_{||} = \rho_p d_p^2 Q/18\eta {W_{||}}^2 H$, where ρ_d is the particle density, and d_p is the particle diameter) is calculated in the order of O(10^{-10} – 10^{-8}) which means that the particles follow fluid streamlines closely.

To analyze the effect of the hydrodynamic stress on the particle deposition and the pore clogging, the hydrodynamic stress at each condition is calculated. Stress (σ) is calculated as the product of the medium shear viscosity (η) and the characteristic shear rate ($\dot{\gamma}$) calculated from the flow rate. The shear rate within the channel at each flow rate is calculated as $\dot{\gamma} = 2\bar{V}/W_{||} = 2Q/H{W_{||}}^2$ [74]. The range of the hydrodynamic stress covered in this study is about 1.9 ~ 42.1 Pa, and the stress

according to each medium viscosity and flow rate can be confirmed in **Table 4**.

Table 3. Formulation of the samples and dimensionless parameters at each flow conditions

Fluid	PS [wt%]	Glycerol [wt%]	Q [mL/hr]	Re	St
Gly50PS	0.1	50	$0.7 \leq Q \leq 1.7$	$0.43 \leq Re \leq 1.04$	$O(10^{-10} - 10^{-8})$
Gly60PS		60		$0.25 \leq Re \leq 0.61$	
Gly70PS		70		$0.13 \leq Re \leq 0.31$	
Gly80PS		80		$0.05 \leq Re \leq 0.13$	

Table 4. Shear viscosity and hydrodynamic shear stress at each flow rate conditions of glycerol solution.

Fluid	η [mPa · s]	σ [Pa]				
		Q = 0.7 [mL/hr] ($\dot{\gamma}$ = 388.9 [1/s])	1.0 (555.6)	1.2 (666.7)	1.5 (833.3)	1.7 (944.5)
Gly50PS	5.1	1.9	2.8	3.4	4.2	4.8
Gly60PS	8.9	3.5	4.9	5.9	7.4	8.4
Gly70PS	17.7	6.9	9.8	11.8	14.8	16.7
Gly80PS	44.6	17.3	24.8	29.7	37.2	42.1

3.3. Results and discussion

3.3.1. From particle deposition to pore clogging

The particle deposition behavior in the cross-end single pore implemented by the T-shaped microchannel is observed by a CCD camera. The image is taken from the center plane of the position in the channel height direction. **Fig. 3.3** shows the particle deposition process at a flow rate of 1.2 mL/hr for the Gly60PS sample. The dark area near the channel wall in **Fig. 3.3** represents the particle deposition. When the fluid flows through the T-junction, edge deposition occurs, in which the particles begin to accumulate on the edge region indicated by the red color on the right (**Fig. 3.3a**). After a while, the particle deposition also occurs at the edge marked in blue color on the opposite side. This edge deposition occurs at the beginning of the experiment under all conditions regardless of the glycerol concentration and flow rate. After that, the cluster of edges gradually grows into a larger form due to continuous particle deposition over time (**Fig. 3.3b**). During this process, a rolling phenomenon is also observed, in which the particles newly approaching the deposited particle layer due to the flow are stuck temporarily and detached, and then, the particle rolls over the deposition layer. This rolling was also demonstrated by Kim *et al*. [41].

Along with the rolling phenomena, an agglomerate breakup is also observed, which the growing cluster is completely broken up due to the flow (**Fig. 3.4**). In **Fig. 3.4**, the end of agglomerate breaks up and disappears. After that, as more time passes, the size of the cluster that grows larger and larger due to the successive particle deposition becomes comparable to the trans-stream width of the channel ($W_{\perp}$), and pore clogging blocking the pores connected to the $\mathrm{Outlet}_{\perp}$ occurs (**Fig. 3.3c**). Uniquely,

such pore clogging is observed only at specific glycerol concentrations and flow rates, unlike the edge deposition (**Fig. 3.3a**), growth of deposition (**Fig. 3.3b**), rolling, and agglomerate breakup (**Fig. 3.4**) observed under all experimental conditions.

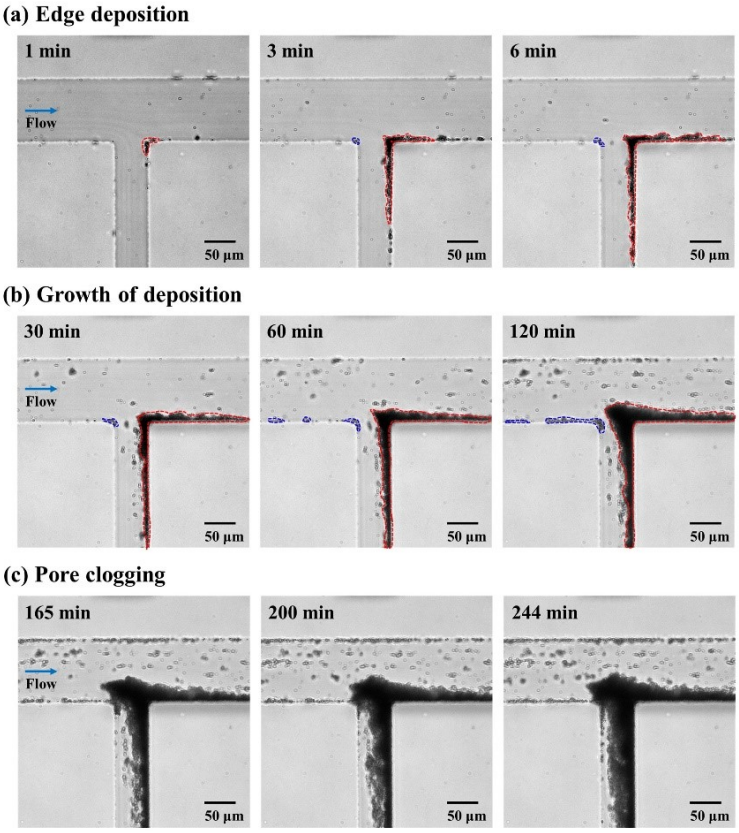

Fig. 3.3. Particle deposition behavior of Gly60PS at Q = 1.2 mL/hr: (a) Snapshots of edge deposition, (b) growth of deposition, and (c) pore clogging. Particle deposition are outlined with red and blue.

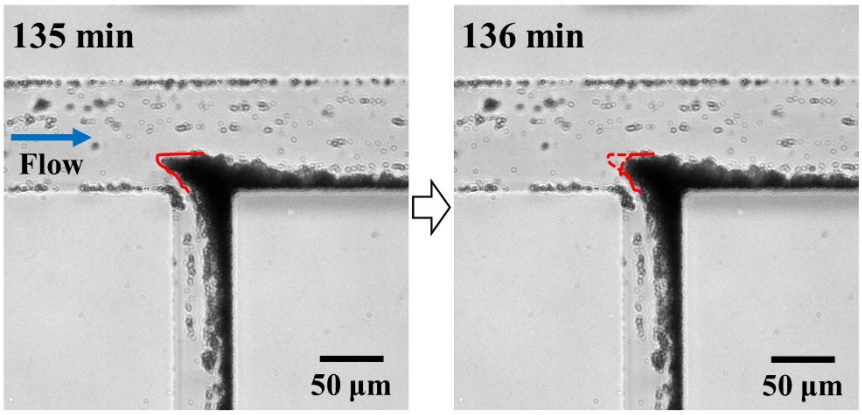

Fig. 3.4. Agglomerate breakup of Gly60PS at Q = 1.2 ml/hr. The snapshots are captured at 135 min.

Fig. 3.5 shows the particle deposition state of Gly60PS and Gly80PS when the experiment is finished by injecting the total sample volume (5 mL) of the syringe at the same flow rate. Even though the fluid is injected at the same flow rate, the particle deposition behavior of the two samples is dramatically different. Pore clogging occurs with Gly60PS at a low glycerol concentration (**Fig. 3.5a**); however, pore clogging does not occur with GlyPS80 at a higher glycerol concentration (**Fig. 3.5b**). Although the focal depth observed is the central plane of the channel, it is impossible to accurately determine whether the three-dimensional channel is fully clogged because it is a two-dimensional image. Thus, it should be noted that the fluid can possibly flow through pores that are not completely blocked. However, when observed at various focal depths, the difference in the deposition behavior in the height direction is not significant. The clogging is defined in the next section. **Fig. 3.6** shows the overall pattern of the clogging behavior according to the glycerol concentration and the flow rate. In the case of Gly50PS and Gly60PS, pore clogging occurs due to the particle clusters at all flow rates, and in the case of Gly70PS, the clogging occurs only under a flow rate of 0.7 mL/hr, but it does not occur at other flow rates. Gly80PS, which has the highest glycerol concentration, does not cause clogging at all tested flow rates. In other words, as the flow rate and the glycerol concentration increase, the threshold for clogging to occur is not reached, and accordingly, it can be confirmed that there are conditions in which clogging takes place.

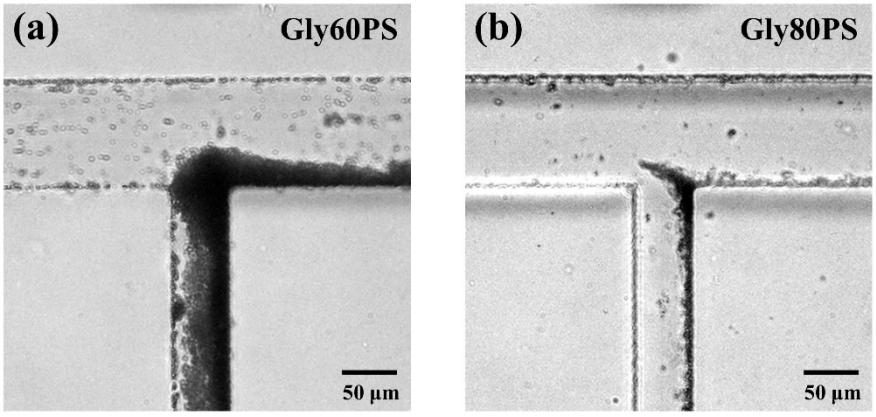

Fig. 3.5. Comparison of particle deposition between (a) Gly60PS and (b) Gly80PS when the flow rate is 1.2 mL/hr.

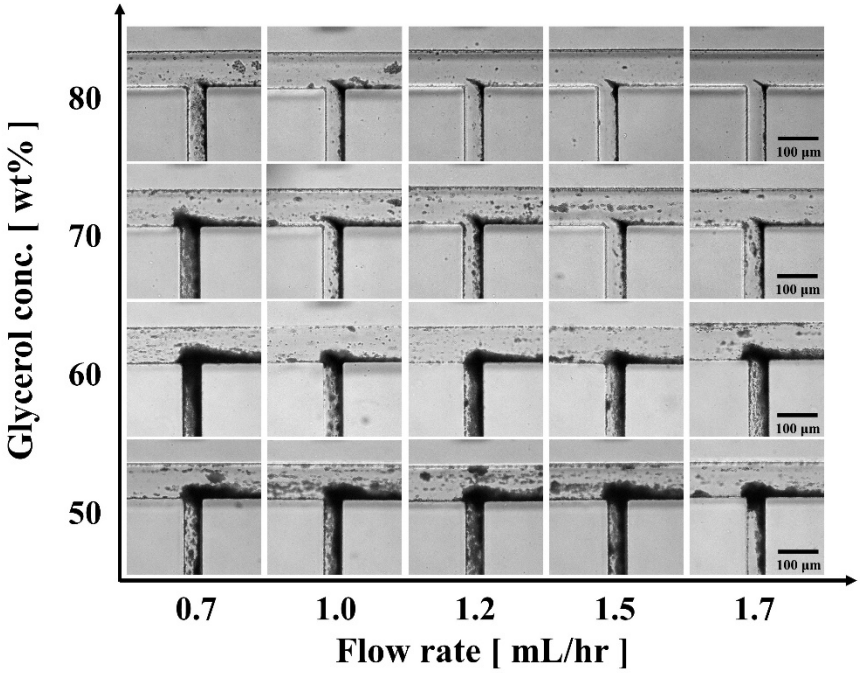

Fig. 3.6. Overall tendency of clogging behavior depending on flow rate and glycerol concentration. All images are taken when the injected sample volume is 5 mL.

3.3.2. Quantification of clogging: Blockage ratio and Deposition ratio

To quantify the observed particle deposition and define the pore clogging, the captured images are converted into binary images through image processing, and the number of black pixels in the channel is counted. Through this process, the change in the ratio of the pore width due to successive particle deposition over time and the change in the ratio of the particle deposition area accumulated in the channel are quantified. **Fig. 3.7** shows the blockage ratio (L^*) and the deposition behavior according to the injected sample volume ($V_{injected}$). As shown in the inset image of **Fig. 3.7a**, the blockage ratio (L^*) is defined as a value subtracted from 1 after normalization by dividing the width of the trans-stream entrance (L) connected to the $\mathrm{Outlet}_{\perp}$ over time by the initial width of the trans-stream (L_0). That is, the blockage ratio (L^*) has a value between 0 and 1, where $L^* = 0$ means that the particle deposition does not occur at the pore entrance, and $L^* = 1$ means that the pore entrance is fully blocked due to the particle deposition. As mentioned above, there is a limitation in not being able to check the whole depth of the channel, so the pores may not be completely blocked. However, when observed at various focal depths, the difference in the deposition behavior in the height direction is again not significant. In **Fig. 3.7a**, L^* reached 1, and it is confirmed that the pore is blocked when the injected volume is 0.8 mL. **Fig. 3.7b** shows the deposition behavior at specific injection time and volume. When 0.47 mL of the sample is injected (**Fig. 3.7b (1)**), L^* is about 0.8 meaning 80 % of the pore entrance is blocked, and when 1.17 mL of sample is injected (**Fig. 3.7b (2)**), L^* is 1 indicating the pore is apparently blocked. Interestingly, even after L^* reaches 1, a slight change in L^* is observed at the points where the injected volume is near 3.5, 3.9, and 4.5 mL. The reason is that the

agglomerate, which is blocking the pore, is broken up, and the pore is temporarily reopened shown in **Fig. 3.4**. In **Fig. 3.7b (3)** and **(4)** it can be confirmed that the agglomerate that blocked the pores is broken up and the pore is reopened within 1 minute, resulting in a slight increase of L^* at $V_{injected} = 3.9$ mL show in **Fig. 3.7a**.

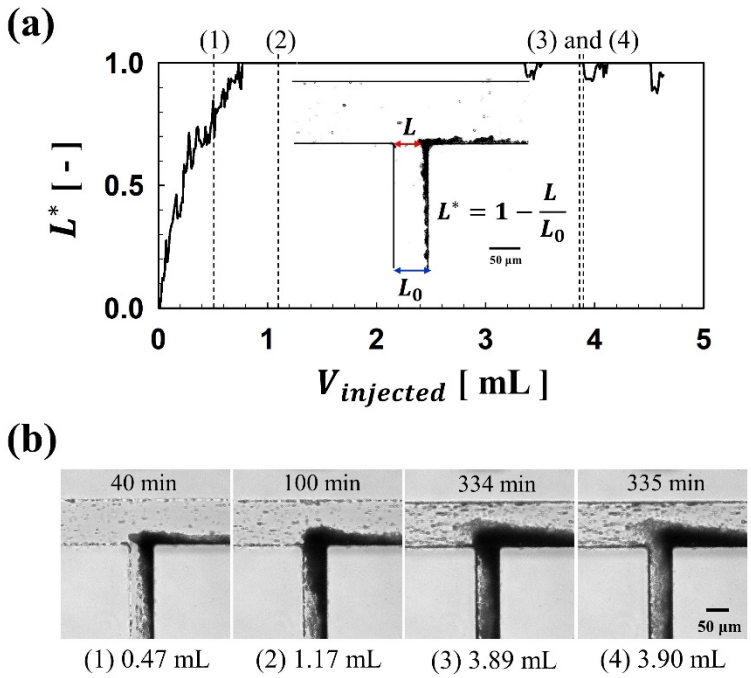

Fig. 3.7. (a) Image processing and blockage ratio (L^*) of Gly60PS. The inset image shows the definition of blockage ratio (L^*). (b) Snapshots of the channel at specific time and injected sample volume.

Fig. 3.8 shows the change in the blockage ratio (L^*) according to the injected sample volume ($V_{injected}$) under all experimental conditions. In the case of Gly50PS, L^* reaches 1 under all flow rate conditions (**Fig. 3.8a**). In the slowest flow rate condition q0.7, L^* reaches 1 when the injected volume is 1 mL, and as the flow rate increases, the injected volume at $L^* = 1$ increases. In all flow rate conditions, L^* of Gly50PS reaches 1 when the injected volume is between 1 and 2.5 mL. Similarly, in the case of Gly60PS (**Fig. 3.8b**), L^* eventually reaches 1 under all flow rate conditions, and as the flow rate increases, the value of the injected volume that flows until L^* reaches 1 tends to increase. In all flow rate conditions, L^* of Gly60PS reaches 1 when the injected volume is between 1.8 and 4.8 mL. On the other hand, a different result is observed in Gly70PS. As shown in **Fig. 3.8c**, in Gly70PS, L^* reaches 1 only under the lowest flow rate conditions, and L^* does not reach 1 in the remaining 4 flow rate conditions. The injected volume when L^* reaches 1 at q0.7 is 4 mL. In experiments with q1.0 and faster flow rate, L^* tends to gradually increase and then converges to a constant value after a certain injected volume. Additionally, the converging value of L^* decreases as the flow rate increases. That is, when the fluid flows at 0.7 mL/hr in Gly70PS, the particle deposition proceeds actively and the pore entrance is clogged; however, when the flow rate is increased to 1.0 mL/hr or more, the pore entrance is not completely clogged, and L^* remains constant. This result indicates that the ratio of the particle deposition area among the pore width decreases as the flow rate increase. In the case of Gly80PS (**Fig. 3.8d**), L^* does not reach 1 under all flow conditions. Furthermore, as the flow rate increases, the converging value of L^* tends to decrease similar to the results of Gly70PS (**Fig. 3.8c**). Therefore, it can be confirmed that the particle deposition is inhibited as the flow rate increases.

Fig. 3.8 can be considered according to the glycerol concentration at the same flow rate. For example, L^* reaches 1 at 1 mL of the injected volume with Gly50PS of q0.7, and as the glycerol concentration gradually increases, the injected volume until $L^* = 1$ tends to increase. Finally, L^* does not reache 1 in Gly80PS. Because the increase in the glycerol concentration is the same as an increase in the medium viscosity, it can be interpreted that as the medium viscosity increases, even at the same flow rate, the injected volume until $L^* = 1$ increases. Furthermore, under a flow rate in which L^* does not reach 1, the converging value of L^* decreases as the medium viscosity increases. In other words, it can be confirmed that as the medium viscosity increases, the particle deposition is inhibited.

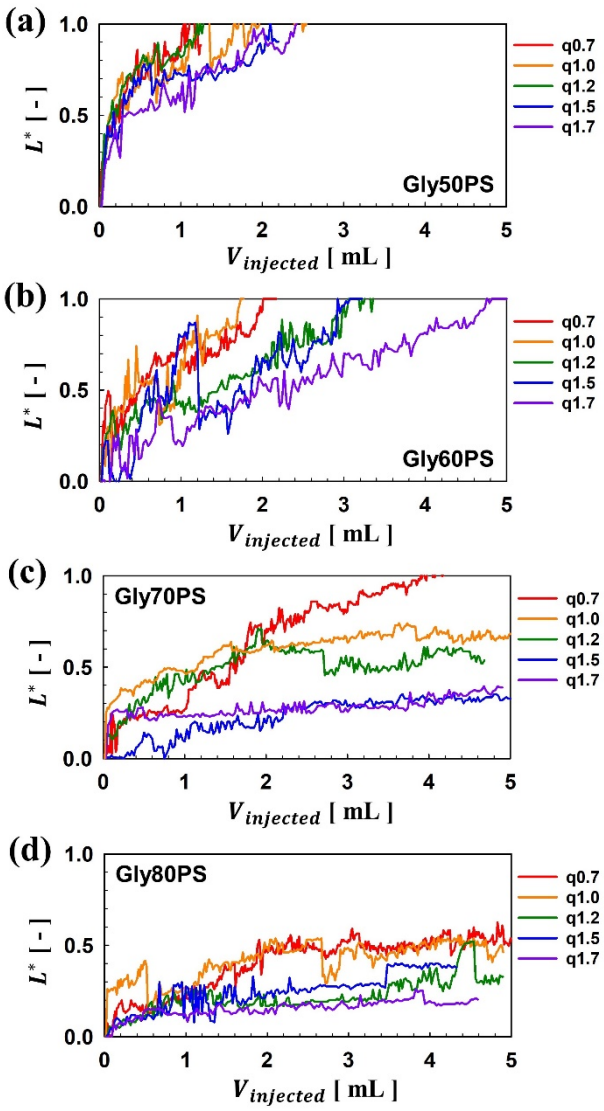

Fig. 3.8. Blockage ratio (L^*) according to the injected sample volume ($V_{injected}$) at each glycerol solution and flow rate: (a) Gly50PS, (b) Gly60PS, (c) Gly70PS, and (d) Gly80PS.

In addition to the blockage ratio (L^*), the particle deposition is quantified by calculating the ratio of the particle deposition area in the channel. **Fig. 3.9** shows the change in the deposition ratio (A_d^*) according to the injected volume ($V_{injected}$) under all experimental conditions. The deposition ratio is defined and calculated as shown in the inset image of **Fig. 3.9a**. The deposition ratio (A_d^*) is the ratio of the particle deposition area (A_d: area of the deposition shown in black color) to the area that includes both the trans-stream and cross-stream (S: shaded area shown in grey color). The particle deposition area (A_d) is calculated by counting the number of black pixels in the binary image converted by the image processing as mentioned before. That is, when A_d^* is 1, it means that the particle deposition occurs in all areas of the trans-stream and cross-stream, and when A_d^* is 0, it means that there are no deposited particles. Under all flow rate conditions of Gly50PS in **Fig. 3.9a** and Gly60PS in **Fig. 3.9b**, A_d^* increases as the injected volume increases, and in general, the faster the flow rate is, the smaller the A_d^* value is when the injected sample volume is identical. The continuous increase in A_d^* as the injection of samples can be interpreted that the number of accumulated particles is greater than the number of that broken up. Meanwhile, in the cases of Gly70PS (**Fig. 3.9c**) and Gly80PS (**Fig. 3.9d**), even if the injected volume increases at the fast flow rate conditions, A_d^* does not increase significantly anymore. The converging value of A_d^* indicates an equilibrium between the number of accumulated particles and the number those that are broken up and flowing. By comparing the values of A_d^* at the same flow rate and injected volume according to the glycerol concentration, it is confirmed that as the glycerol concentration increases, the value of A_d^* decreases. In other words, as the medium viscosity increases, less particle deposition occurs when the same volume of the fluid flows. Therefore, similar to the results of the blockage ratio (L^*), the particle

deposition is inhibited as the flow rate and medium viscosity increase.

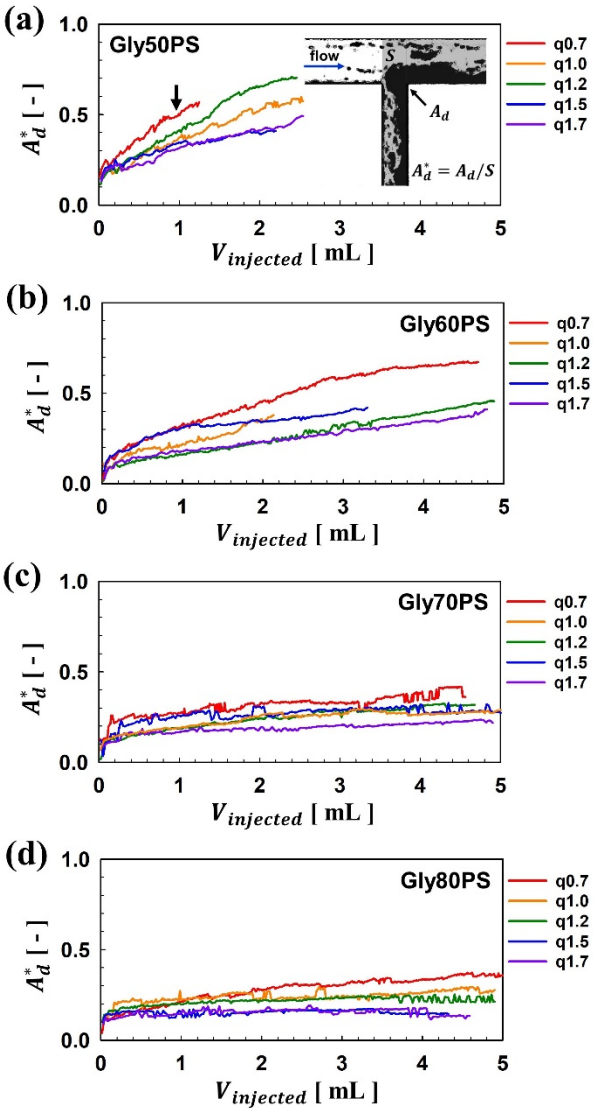

Fig. 3.9. Deposition ratio (A_d^*) according to the injected sample volume ($V_{injected}$) at each glycerol solution and flow rate: (a) Gly50PS, (b) Gly60PS, (c) Gly70PS, and (d) Gly80PS. The inset image shows the definition of deposition ratio and the representative images of Gly50PS q0.7 sample at 1 mL of injected volume (marked with black arrow).

3.3.3. Critical stress and phase diagram of clogging

To comprehensively investigate the effect of the hydrodynamic stress on the particle deposition in each experimental condition, the observed experimental results are shown together with the hydrodynamic stress (σ). **Fig. 3.10** shows the particle deposition behavior and the phase diagram according to the stress. To define the pore clogging in the T-shaped channel, the final blockage ratio (L_f^*) at $V_{injected} = 5$ mL is measured. **Fig. 3.10a** shows the final blockage ratio (L_f^*) according to the stress. Under the conditions of the weak stress, L_f^* reaches 1, but under the strong stress conditions, L_f^* does not reach 1 and decreases with the stress. Here, we defined the situation where L_f^* does reach 1 as "clogging", and the situation where L_f^* does not reach 1 is defined as "no clogging". Thus, "clogging" occurs below a specific stress value, but "no clogging" occurs above a specific stress value. These results suggest that there is a critical stress level that causes the clogging. In this study, the value of the critical stress ($\sigma_{critical}$) is observed at approximately 9 Pa. The possibility of the existence of the critical stress that determines the clogging has also been reported in another study that observed clogging in contraction channels [41]. The critical stress can be affected by several factors, such as the medium viscosity, colloidal interaction between particles, particle-wall interaction, and kinematics in the flow geometry. In this study, the clogging is inhibited when the stress is greater than the critical stress.

In addition to the determination of the clogging, the degree of the particle deposition also varies depending on the critical stress. **Fig. 3.10b** shows the change of the deposition ratio (A_d^*) until a 1 mL sample volume is injected. To quantify the particle deposition at the beginning of the flow according to the hydrodynamic stress, the change in A_d^* up to the corresponding injection volume is investigated. Thus, a

1 mL sample volume is a value defined to exclude the effect of the flow field that changes due to the deposited particle layer and effectively shows a competition between the adhesion force of the particles and the desorption force due to the flow at the initial stage of the flow. The change of the deposition ratio until the 1 mL injection volume ($\Delta A_d^*|_{V_{injected}\,=\,1\,\mathrm{mL}}$) shows two kinds of tendencies according to the stress. In the stress range before the critical stress (about 9 Pa in this study), it shows a gradual decrease according to the stress and shows no significant change in the range above the critical stress. In other words, in a region where the stress is smaller than the critical stress, it can be interpreted that the larger the stress is, the more the overall particle deposition is inhibited, and it can be seen that the inhibitory effect is saturated above the critical stress. Therefore, in **Fig. 3.10a** and **3.10b**, it is confirmed that the presence of the critical stress, which determines whether clogging is formed, and the fact that the behavior of the particle deposition depending on the stress are significantly different.

Fig. 3.10c shows the phase diagram of the clogging, which is defined in **Fig. 3.10a**, in the entire experimental condition. As the flow rate and medium viscosity increase, the particle deposition is inhibited, and the clogging does not occur, and it is confirmed that this effect depends on the stress.

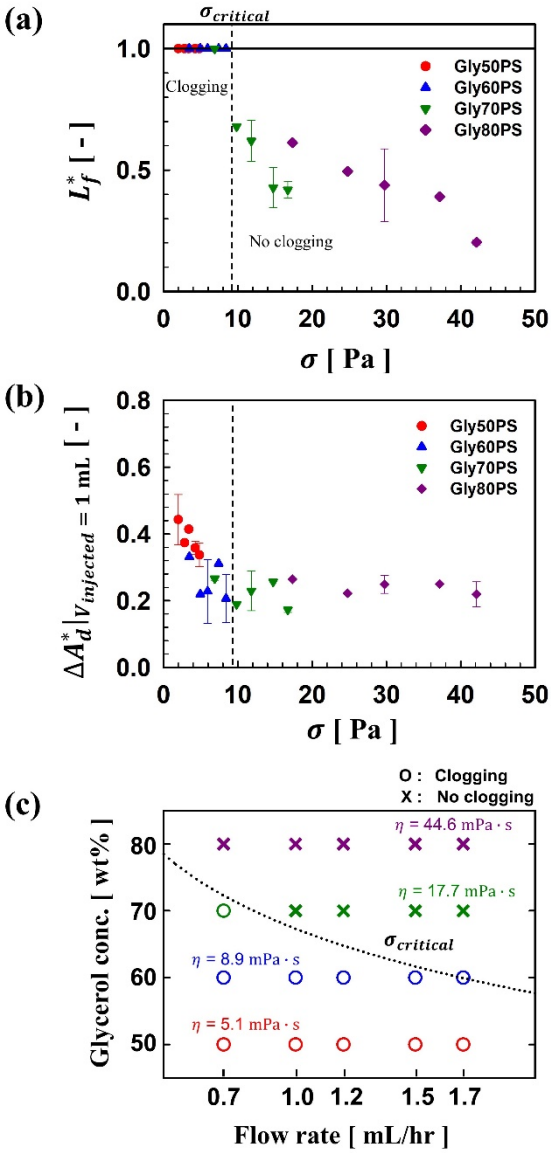

Fig. 3.10. (a) Final blockage ratio (L_f^*) at each stress. Stress (σ) are calculated from the product of the shear rate ($\dot{\gamma}$) and shear viscosity (η) of the sample. (b) Change of deposition ratio (ΔA_d^*) up to 1 mL of injected volume ($V_{injected}$) versus stress (σ) of Gly50PS, Gly60PS, Gly70PS, and Gly80PS (c) Phase diagram of clogging at each conditions. The dotted line is the iso-stress line equal to the critical stress value.

3.3.4. Ratio of the hydrodynamic stress to the colloidal interaction

In the previous Section 3.3.3, the presence of the critical stress in the particle deposition process is confirmed. The critical stress observed in this study is about 9 Pa, as mentioned earlier. To validate these critical stress values, the dimensionless quantity, M', in which the ratio of the hydrodynamic drag force to the maximum attractive interparticle force, is considered. The variables controlled in this study are the medium viscosity and flow rate of the sample. The samples made of four glycerol concentrations can apply the different hydrodynamic stresses according to the flow rate, which causes the different drag forces to act on the particle deposition process. On the other hand, as mentioned in Section 3.2.1, the interparticle force does not change significantly under the experimental conditions used in this study. Thus, the effect of hydrodynamic drag force is discussed only, and not the effect of the interparticle force. Nevertheless, the colloidal interaction is accurately calculated by reflecting the small effects of the glycerol concentration (permittivity, zeta potential). In summary, M', a non-dimensional number representing the balance between the drag and the interparticle force, is investigated by changing the flow rate and the glycerol concentration. M' is called the Mason number and defined as Eq. (11) [75, 76].

$$M' \equiv \frac{6\pi\eta\dot{\gamma}R^2}{F_i} \tag{11}$$

where R is the radius of the particle, and F_i is the maximum attractive force between the particles. The product of the medium viscosity (η) and shear rate ($\dot{\gamma}$) in

the hydrodynamic drag force due to the flow can be regarded as the hydrodynamic stress (σ). The numerator of the Eq. (11) is the hydrodynamic drag force

F_i is obtained from Eq. (12) through the differential slope of the colloidal interaction potential curve using DLVO theory:

$$F_i = \left(\frac{dU}{dh}\right)_{max} \tag{12}$$

where U is the particle-particle DLVO potential expressed as a function of the surface separation distance h.

The particle-particle interaction potential (U) is evaluated as the sum of the van der Waals interaction and the electrostatic double layer interactions [20]:

$$U = U_{vdW} + U_{el} \tag{13}$$

where U_{vdW} is the van der Waals attraction potential, and U_{el} is the electrostatic double layer potential. The detailed processes of calculating U_{vdW} and U_{el} are similar with Section 2.3.1 and the calculated particle-particle interaction potential curve is show in the **Fig. 3.11**. Only the equation of U_{vdW} and U_{el} are changed slightly (Eq. (14) and (15)) and γ_0 is same as Eq. (4).

$$U_{vdW} = -\frac{A}{6}\left[\frac{2}{l^2-4} + \frac{2}{l^2} + \ln\left(1 - \frac{4}{l^2}\right)\right] \tag{14}$$

$$U_{el} = \frac{32\pi\varepsilon R k_B^2 T^2 \gamma_0^2}{Z^2 e^2} exp(-\kappa R(l-2)) \tag{15}$$

where U_{vdW} is the van der Waals attraction potential, U_{el} the electrostatic double layer potential, A the Hamaker constant, $l = r/R$ (r the center-to-center interparticle distance, R the radius of the particle. Note that $h = (l - 2)r$.), ε the medium permittivity, k_B the Boltzmann constant, T the absolute temperature, e the elementary charge, ψ_0 the surface potential, κ the inverse of the Debye length, and Z the counter-ion charge. The parameters are provided in **Table 5**.

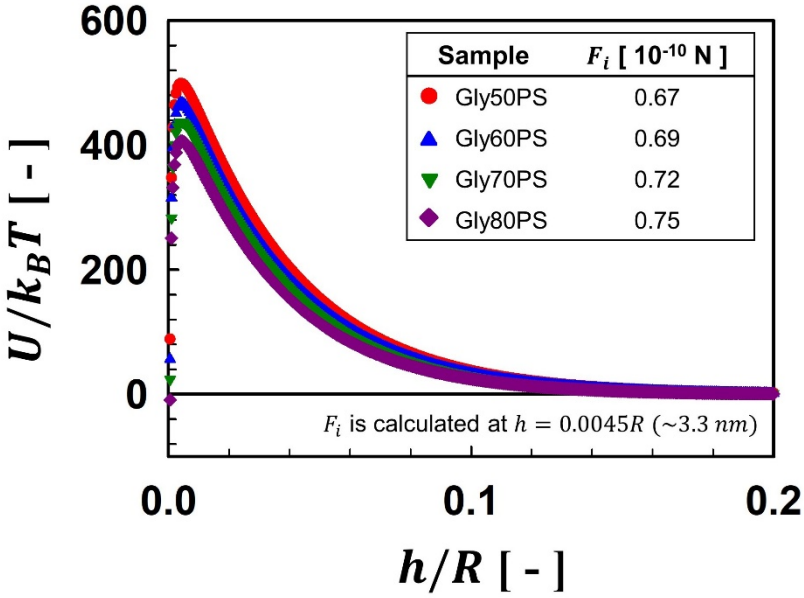

Fig. 3.11. Particle-particle DLVO interaction potential (U). h is the surface separation distance between the particles. The inset table is maximum attractive interaction force (F_i) calculated at $h = 0.0045R$.

Table 5. DLVO parameters of each glycerol solution

Parameter	Description	Value
R	Radius of particle [μm]	0.75
ε	Medium permittivity [F/m]	5.63×10^{-10} (Gly50) 5.34×10^{-10} (Gly60) 5.04×10^{-10} (Gly70) 4.75×10^{-10} (Gly80)
T	Absolute temperature [K]	298.15
k_B	Boltzmann constant [J/K]	1.4×10^{-23}
A	Hamaker constant [J]	1.3×10^{-20}
ψ_0	Surface potential [mV]	-32
e	Elementary charge [C]	1.602×10^{-19}
Z	Counter-ion charge [-]	1
κ^{-1}	Debye length [nm]	27.2 (Gly50) 26.4 (Gly60) 25.7 (Gly70) 24.9 (Gly80)

To obtain the maximum attractive force between particles, the differential value of the potential energy is calculated at a distance away from the particle by the surface roughness, where the separation h is minimal. The PS particles used in this study have a very soft surface, and the root mean square roughness ($\overline{R_a}$) measured by atomic force microscopy (AFM), NX-10 (Park Systems, Korea), is about 3.3(±0.8) nm (**Fig. 3.12**). This is equivalent to about 0.45% of the particle radius. The measured roughness is similar to that of Hülagü, D. *et al*. [77] in which the roughness of the PS particle was measured with electron microscopy. Based on the results obtained from Hülagü, D. *et al*. [77], the roughness of PS particle with a diameter 1.8 μm was about 4 nm. Therefore, in this study, F_i is calculated as the differential slope value of U at about $h = 0.0045$R.

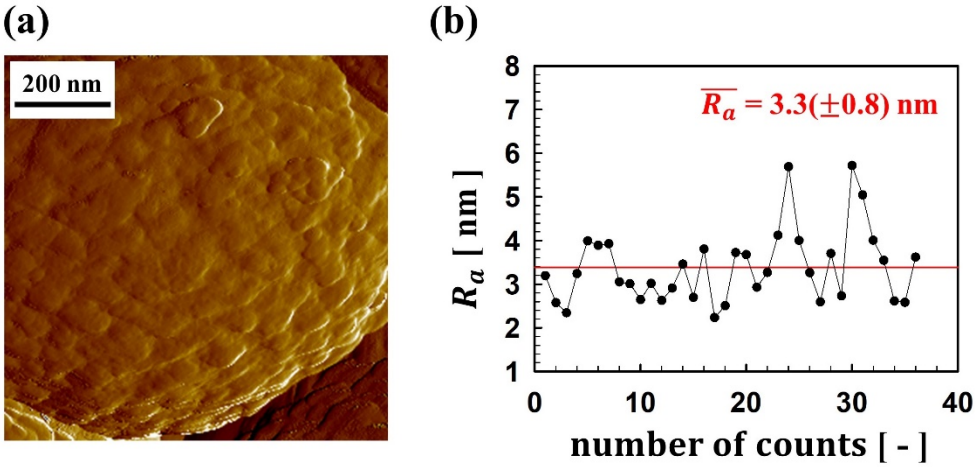

Fig. 3.12. (a) AFM image of PS particle. (b) Surface roughness ($\boldsymbol{R_a}$) of the PS particle measured by AFM. Root mean square surface roughness ($\overline{\boldsymbol{R_a}}$) is calculated from the roughness of about 40 random positons on particle surface.

Fig. 3.13 shows the change of M' according to the hydrodynamic stresses in this study. As mentioned earlier, M' is the ratio of the hydrodynamic force (F_h) to the maximum attractive interaction force (F_i), which is a non-dimensional number for the ratio of the two forces affecting the adhesion of the particles. That is, a value of M' greater than 1 means that the hydrodynamic force due to the flow is more dominant, and a value of M' less than 1 means that the attraction force due to the interaction between the particles is more dominant. The hydrodynamic force is a drag force that sweeps the particles away from the walls, or the piled particles agglomerate or cluster, and it is a force that acts in a direction that inhibits the particle deposition. The calculated M' increases almost linearly according to the stress. This is because the colloidal interaction is not significantly affected by the experimental conditions. The relative permittivity value exhibits only minor changes due to the variations in the glycerol concentration, whereas the hydrodynamic force is heavily influenced by both the flow rate and the viscosity of the medium. The attractive interaction force varies from about 0.67×10^{-10} ~ 0.75×10^{-10} N according to the glycerol concentration (inset table of **Fig. 3.11**), and the hydrodynamic force varies from about 0.21×10^{-10} ~ 4.47×10^{-10} N according to the flow condition (**Fig. 3.14**). The value of M' at the critical stress that determines pore clogging observed in this study is about 1.4. In other words, at the critical stress, F_h acting in the direction of inhibiting particle deposition and F_i acting in the direction of promoting the particle deposition are almost comparable. Therefore, it can be interpreted that pore clogging occurs in the range where the interparticle attractive interaction force acts greater than the hydrodynamic drag force. In contrast, pore clogging is prevented in the region where the hydrodynamic stress increases and the drag force becomes dominant over the attractive interaction force. Furthermore, the critical stress can be determined in a

stress region where the magnitudes of the two forces are comparable. In summary, M' can serve as an indicator for detecting the pore clogging in the T-shaped microchannel geometry studied here and can also justify the existence of the critical stress. By utilizing M', clogging issues can be predicted and prevented in advance; additionally, it enables the setting of possible process conditions.

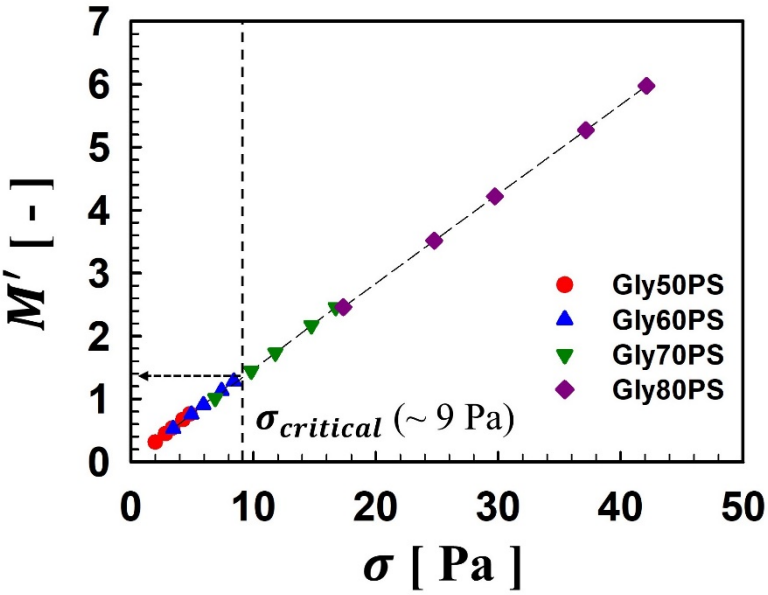

Fig. 3.13. Non-dimensional number (M') according to stress (σ) M' is the ratio of the hydrodynamic force to attractive interaction force.

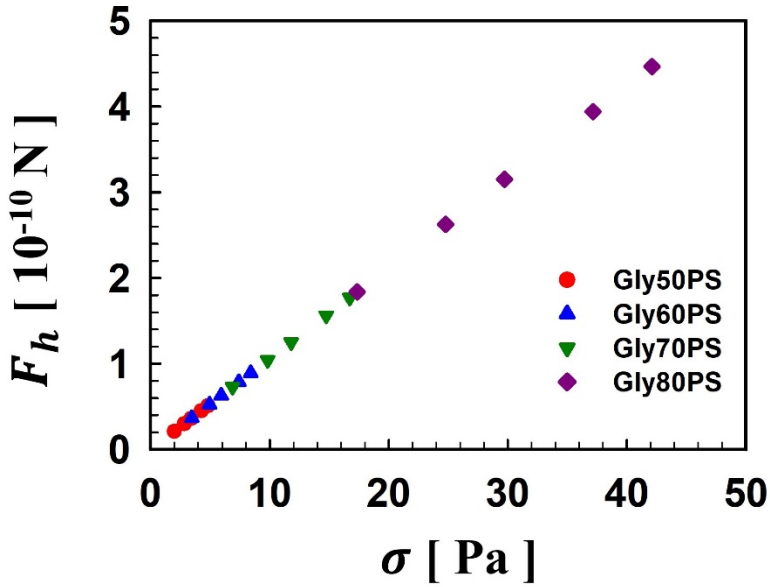

Fig. 3.14. Hydrodynamic force (F_h) according to stress (σ)

3.3.5. Clogging dynamics under critical stress

So far, the behavior of the particle deposition according to the stress and the presence of critical stress have been analyzed and discussed. In this section, we will analyze and discuss the dynamics of the pore clogging in the stress region below the critical stress. To analyze the pore clogging, only the experimental samples below the critical stress are measured for the time and volume required for the clogging to occur. As mentioned earlier, in this study, clogging is defined as the case where the blockage ratio (L^*) (**Fig. 3.8**) reaches 1. Accordingly, we define the clogging time (t_{clog}) as the time taken until the clogging and the clogging volume (V_{clog}) as the injected volume of the sample that led to the clogging.

Fig. 3.15 shows the results of the time when the clogging occurs according to the stress. In **Fig. 3.15a**, the average clogging time (t_{clog}) changes according to the stress. However, when the time is multiplied by the flow rate and replaced with the injected volume until the clogging occurred, the average clogging volume (V_{clog}) increases with the stress. To explain this aspect, the number of particles injected into the channel until the clogging is calculated with V_{clog}. The number of particles required to clog (N_{clog}) is calculated with Eq. (16):

$$N_{clog} \simeq \frac{t_{clog} Q \phi}{v_p} = \frac{V_{clog} \phi}{v_p} \tag{16}$$

where v_p is the volume of the PS particle, ϕ is the particle volume fraction, and $V_{clog} = t_{clog} Q$. **Fig. 3.15b** shows the relationship between the stress and N_{clog}. As the stress increases, the number of particles required until clogging increases

exponentially. It can be fitted in the exponential form, $N_{clog} = a \cdot e^{b \cdot \sigma} + c$. The values of the fitting parameter a, b, and c are 1.95×10^8, 0.28, and 3.78×10^8, respectively.

There are several research results from previous studies on the number of particles required for clogging. A study conducted by H. M. Wyss *et al*. [78] is considered a pivotal contribution to research on clogging mechanisms in microchannels. They confirmed the particle number required until clogging exists which is independent of the particle volume fraction. Furthermore, they observed that it is scaled by the ratio of the length scale of the channel geometry and the particle diameter. In other words, it can be considered that there is a critical particle number required for pore clogging shown in this study as well. It is noteworthy that this number of particles can be changed by the hydrodynamic stress due to the flow. As the stress acting in the direction of inhibiting particle deposition increases, the rolling and agglomerate breakup phenomena become more frequent, and more numbers of particles must flow until eventually clogging occurs. In summary, in fixed channel geometries and particle volume fractions, greater stress leads to an increased requirement for the number of particles for clogging to occur.

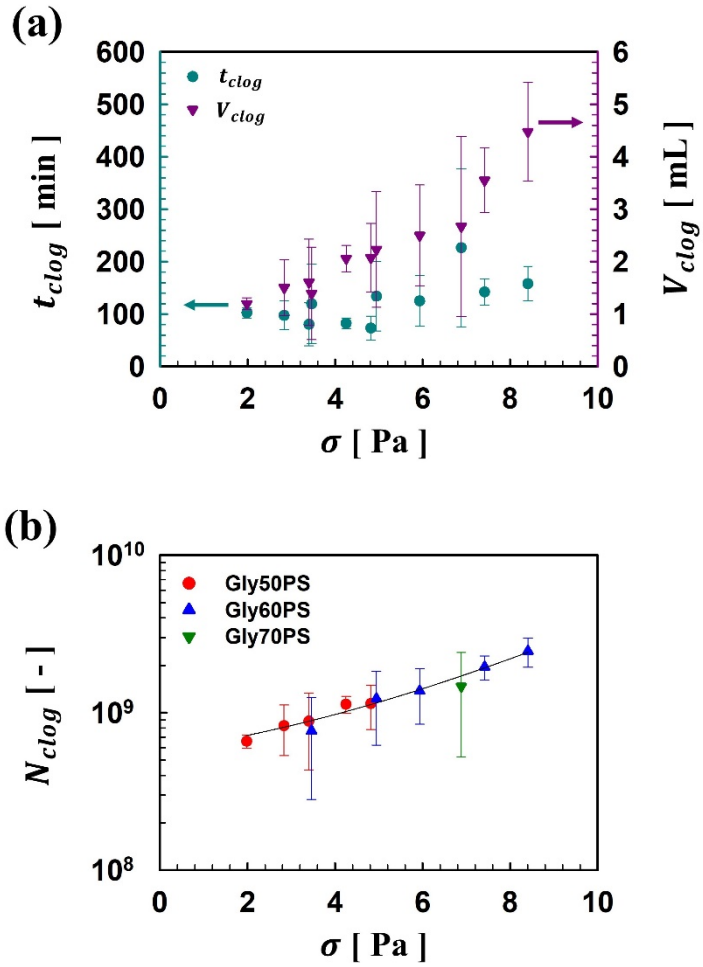

Fig. 3.15. (a) Dependence of clogging time (t_{clog}) and clogging volume (V_{clog}) required to pore clogging on each stress. (b) Total number of particles that flow through channel prior to clogging (N_{clog}) as a function of stress.

3.4. Conclusions

In this chapter, the mechanism for the deposition of PS particles dispersed in glycerol solutions and the pore clogging is investigated in a cross-flow through a T-shaped microchannel. To analyze the effect of the hydrodynamic stress on the clogging mechanism, a systematic experiment is conducted by controlling the flow rate and glycerol concentration. In addition, the particle deposition process is observed through a flow visualization setup with microfluidics, and the clogging is quantified by image processing.

The clogging process due to the continuous particle deposition is observed step by step. First, when a suspension is injected into the T-shaped channel, the “edge deposition” step starts where the particles deposit on the junction edge connected to the two outlets. After that, starting from the edge part, the particles continuously accumulate to form an agglomerate and progress to “growth of deposition” where an agglomerate gradually grows. During the process of the growing agglomerate, a “rolling” phenomenon is observed in which the particles that are temporarily stuck can roll due to the flow. Moreover, an “agglomerate breakup” phenomenon is observed where the growing agglomerate falls off. These repeating attachment and detachment processes result in two distinct deposition outcomes. The pore of the trans-stream can either become clogged or remain unclogged, depending on the flow rate and the medium viscosity. As the flow rate and the medium viscosity increase, there is a tendency for “no clogging” to occur.

The pore clogging observed in this study is analyzed quantitatively with the blockage ratio and the deposition ratio. The stress is calculated with the flow rate and the viscosity of the glycerol solution. Consequently, it is confirmed that the blockage

ratio and the deposition ratio change with the injected volume before and after the specific critical stress value. As the stress increases, the blockage ratio does not reach 1, and the deposition area decreases when the same amount of sample is injected. In other words, if the stress is small, the particle deposition is not interrupted, and the particles are easily deposited, and eventually, pore clogging occurs. On the other hand, if the stress is large, clogging does not occur in the channel because the particles are easily washed away. In the end, there is a critical stress that determines whether this clogging occurs. To discuss the critical stress observed in this study, a non-dimensional number expressed as the ratio of the hydrodynamic force and the colloidal interaction force is utilized. As a result, the magnitudes of the two forces have comparable values when the hydrodynamic stress is equal to the critical stress. This means that when the hydrodynamic force, which inhibits the particle deposition, becomes comparable to the attraction force between the particles, the deposition is inhibited, and clogging does not occur. The stress at this point can be expressed as the critical stress. Additionally, under clogging conditions, the time and injected volume until clogging occurs are investigated. No special tendency is observed for the time taken until the clogging occurs, but a significant tendency is observed for the injected sample volume. When calculating the number of particles that flowed to the clogging, it is shown that as the stress increases, the number of particles required to clog also increases because particle deposition is inhibited.

This study identifies the impact and underlying mechanism of the hydrodynamic stress on the particle deposition and the clogging during a cross-flow. In particular, this study is expected to be highly significant as a fundamental analysis of the critical stress and the particle numbers leading to clogging in the basic geometry of a cross-flow which is commonly used in various flow transport and filtration systems.

Furthermore, this study focuses on identifying the particle deposition and clogging in the simplest Newtonian fluid, laying the foundation for future research on more complex fluids with viscoelastic properties. By providing a baseline understanding of these phenomena, this study serves as a critical first step toward comprehending the behavior of particles in a variety of fluid systems. The methodology and findings of this study can aid in the design of flow operating conditions to control particle deposition and clogging in pipes and membranes for various complex fluids. By applying the insights gained from this study, researchers and engineers can develop strategies to mitigate particle-related issues and optimize the performance of fluid transport and filtration systems.

Chapter 4. Concluding remarks

This thesis presents experimental investigations on the dynamics of particle deposition and pore clogging in colloidal suspensions flowing through complex flow. In addition to identifying clogging mechanisms in multi-pore systems as done in previous studies, the present study comprehensively considers colloidal interactions and hydrodynamic stresses to explore particle deposition and pore clogging processes in the simplest single-pore system. As each pore is adjacent to the multi-pore system and can be influenced by nearby particle deposition, it was necessary to identify the mechanism for particle deposition in a single-pore. To achieve this, particle deposition was studied in two fundamental geometries according to the filtration method. Filtration is classified into dead-end flow filtration and cross-end flow filtration based on the positional relationship between the filtering and flow directions. The unit geometry among numerous pores of the membrane was simplified into the contraction and T-shaped geometries, respectively. A contraction channel involves a flow path that rapidly contracts, which can be simplified to the fundamental geometry of dead-end flow filtration and is widely used as a benchmark geometry for various pipe flows. On the other hand, a T-shaped geometry involves two flows, cross-stream and trans-stream, so it can be simplified as the fundamental geometry of cross-end flow filtration, and is a wide-ranging geometry that is also used for flow separation and mixing. Therefore, this thesis analyzes and identifies the effects of colloidal interactions and hydrodynamics in fundamental geometries that simulate two representative filtrations.

Chapter 2 of the thesis describes the experimental study of particle deposition pattern in a 4:1 contraction channel, considering colloidal interaction and

hydrodynamic stress. The colloidal interaction was controlled by varying the salt concentration, and the flow rate was altered. It was observed that the particle deposition pattern changed dramatically with the salt concentration. In the case of a repulsive interaction of 1 mM, particle deposition occurred only downstream, and hardly any deposition occurred upstream under all flow conditions. Conversely, in the case of an attractive interaction of 100 mM, deposition occurred upstream at slow flow rates and in both upstream and downstream at fast flow rates. The difference in particle deposition tendency was explained by the relative ratio of colloidal force and lift force. For the 1 mM sample, the repulsive colloidal force and lift force repelled particles from the wall, thereby inhibiting upstream deposition. However, downstream deposition occurred due to the increased particle flux density. For the 100 mM sample, attractive colloidal force caused upstream deposition, which decreased as the lift force increased in the downstream at higher flow rates. Additionally, sonication was applied to analyze the effect of colloidal size on particle deposition. It was observed that downstream particle deposition increased as colloidal size decreased because lift force decreased when agglomerates of the 100 mM sample were broken up through sonication.

In chapter 3, the focus was on studying the effect of hydrodynamic stress on particle deposition and clogging patterns in a T-shaped microchannel. The flow rate and glycerol concentration were varied to control hydrodynamic stress and particle deposition was observed through the visualization setup used in chapter 2. The study identified the step-by-step process of particle deposition and accumulation, including phenomena such as "edge deposition", "growth of deposition", "rolling", and "agglomerate breakup". Depending on the sustained attachment and detachment of particles, two different deposition outcomes were observed. Additionally, as the flow

rate and glycerol concentration increased, pore clogging was inhibited, leading to "no clogging" outcomes. Image processing was utilized to analyze the observed deposition and clogging patterns. To analyze pore clogging in this study, the blockage ratio and the deposition ratio were used for quantitative assessment. The stress was computed from the flow rate and the viscosity of the glycerol solution. The blockage and deposition ratios behaved differently depending on the volume injected before and after the critical stress. As stress increased, the blockage ratio never reached 1, while the deposition area decreased for the same sample amount. This meant that, at low stress, particles were quickly deposited, eventually leading to pore clogging, while at high stress, particles were easily washed away, preventing clogging in the channel. The critical stress, which determines whether clogging occurs or not, was discussed using a non-dimensional number representing the ratio of hydrodynamic force to colloidal interaction force. At the critical stress, the two forces were comparable, inhibiting deposition and preventing clogging. The study also explored the time and injected volume required for clogging under clogging conditions. The number of particles flowing before clogging increased exponentially with stress.

In this thesis, the various forces involved in the attachment and detachment between particles and the channel wall in complex flows occurring in filtration systems were studied using both contraction and T-shaped geometries. The forces considered included van der Waals and electrostatic interactions, lift and hydrodynamic drag forces, among others. The effect of flow conditions on the balance between these forces was experimentally analyzed, and changes in particle deposition patterns were identified, leading to a better understanding of pore clogging. The insights gained from this research can be applied to various flow systems beyond membrane filtration, as the contraction and T-shaped channels used in this study are

commonly found in liquid phase processes in different industries. For example, the contraction channel is used in coating and ink jetting, while the T-shaped channel is used to merge and divide flow in different directions. The deposition of suspensions over confined geometries is also a ubiquitous phenomenon. Therefore, this thesis not only provides a more fundamental interpretation of membrane filtration clogging but also helps deepen the understanding of particle deposition in various flow systems.

The study of particle deposition in flows still requires significant advancements, and the direction of future researches can be categorized into three main areas. Firstly, progress towards complex fluids is needed as most studies to date have focused on relatively simple fluids with particles dispersed in a simple medium. However, industrial fluids like batteries, CMP slurries, and inks contain polymers or various additives. Thus, it is essential to conduct basic research on particle deposition in fluids with elasticity, yield stress, and shear thinning characteristics. Although adding polymers poses difficulties in considering interactions as adsorption with particles, studying complex fluids is crucial. Secondly, systematic studies of particle deposition in unit geometries are necessary because the transport system in actual processes comprises a combination of simple unit geometries. To understand particle deposition in the entire pipe transport system, studies in individual parts should be conducted. While this thesis discusses contraction and T-shaped geometries, there are various other unit geometries like bending, expansion, and contraction-expansion, and the detailed length scale of the geometry can be adjusted. Despite several unit geometries being available, few studies have been conducted on particle deposition in those environment, making deposition studies in simple unit geometries essential. Lastly, studies of solutions to improve deposition issues are essential. And these studies could be carried out with a study of particle deposition patterns and interpretations in each

unit geometry. In membrane filtration, for example, studies are being conducted to restore the membrane functionality, Similar research needs to be conducted on unit geometry.

In conclusion, this thesis investigated particle deposition in contraction and T-shaped geometries by examining the balance between various forces. The methods and interpretations used in this analysis are important as they establish a foundation for future studies on particle deposition in complex fluids and different unit geometries, and enhance our overall understanding of particle deposition and clogging phenomenon.

Bibliography

[1] J. Zhang, S. Yan, D. Yuan, G. Alici, N.-T. Nguyen, M. Ebrahimi Warkiani, W. Li, Fundamentals and applications of inertial microfluidics: a review, Lab on a Chip, 16 (2016) 10-34.

[2] Q. Zhao, D. Yuan, J. Zhang, W. Li, A Review of Secondary Flow in Inertial Microfluidics, Micromachines (Basel), 11 (2020).

[3] T. Gudipaty, M.T. Stamm, L.S.L. Cheung, L. Jiang, Y. Zohar, Cluster formation and growth in microchannel flow of dilute particle suspensions, Microfluidics and Nanofluidics, 10 (2011) 661-669.

[4] C. Selomulya, G. Bushell, R. Amal, T.D. Waite, Aggregation Mechanisms of Latex of Different Particle Sizes in a Controlled Shear Environment, Langmuir, 18 (2002) 1974-1984.

[5] Y. Kikuchi, H. Yamada, H. Kunimori, T. Tsukada, M. Hozawa, C. Yokoyama, M. Kubo, Aggregation Behavior of Latex Particles in Shear Flow Confined between Two Parallel Plates, Langmuir, 21 (2005) 3273-3278.

[6] Y. Kim, D.Y. Kim, J.S. Hong, K.H. Ahn, Agglomerate Breakup of Destabilized Polystyrene Particles under a Cross-Channel Planar Extensional Flow, Langmuir, 34 (2018) 11454-11463.

[7] N. Shafaei, M. Jahanshahi, M. Peyravi, Q. Najafpour, Self-cleaning behavior of nanocomposite membrane induced by photocatalytic WO3 nanoparticles for landfill leachate treatment, Korean Journal of Chemical Engineering, 33 (2016) 2968-2981.

[8] Y.-J. Won, S.-Y. Jung, J.-H. Jang, J.-W. Lee, H.-R. Chae, D.-C. Choi, K. Hyun Ahn, C.-H. Lee, P.-K. Park, Correlation of membrane fouling with topography of patterned membranes for water treatment, Journal of Membrane Science, 498 (2016) 14-19.

[9] A. Sauret, E.C. Barney, A. Perro, E. Villermaux, H.A. Stone, E. Dressaire, Clogging by sieving in microchannels: Application to the detection of contaminants in colloidal suspensions, Applied Physics Letters, 105 (2014) 074101.

[10] G.H. Goldsztein, J.C. Santamarina, Suspension extraction through an opening before clogging, Applied Physics Letters, 85 (2004) 4535-4537.

[11] C.M. Cejas, F. Monti, M. Truchet, J.-P. Burnouf, P. Tabeling, Universal diagram for the kinetics of particle deposition in microchannels, Physical Review E, 98 (2018) 062606.

[12] D.Y. Kim, S.Y. Jung, Y.J. Lee, K.H. Ahn, Effect of Colloidal Interactions and Hydrodynamic Stress on Particle Deposition in a Single Micropore, Langmuir, 38 (2022) 6013-6022.

[13] J. Lee, S. Sung, Y. Kim, J.D. Park, K.H. Ahn, A new paradigm of materials processing—heterogeneity control, Current Opinion in Chemical Engineering, 16 (2017) 16-22.

[14] P.Z. Çulfaz, S. Buetehorn, L. Utiu, M. Kueppers, B. Bluemich, T. Melin, M. Wessling, R.G.H. Lammertink, Fouling Behavior of Microstructured Hollow Fiber Membranes in Dead-End Filtrations: Critical Flux Determination and NMR Imaging of Particle Deposition, Langmuir, 27 (2011) 1643-1652.

[15] H. Lee, D.-B. Kwak, S.C. Kim, Q. Ou, D.Y.H. Pui, Influence of colloidal particles with bimodal size distributions on retention and pressure drop in ultrafiltration membranes, Separation and Purification Technology, 222 (2019) 352-360.

[16] V. Ramachandran, H.S. Fogler, Multilayer Deposition of Stable Colloidal Particles during Flow within Cylindrical Pores, Langmuir, 14 (1998) 4435-4444.

[17] Y. Li, O. Dahhan, C.D.M. Filipe, J.D. Brennan, R.H. Pelton, Deposited Nanoparticles Can Promote Air Clogging of Piezoelectric Inkjet Printhead Nozzles, Langmuir, 35 (2019) 5517-5524.

[18] D.C. Mays, J.R. Hunt, Hydrodynamic Aspects of Particle Clogging in Porous Media, Environmental Science & Technology, 39 (2005) 577-584.

[19] P. Prakash, A.Z. Abdulla, M. Varma, Contact Force Mediated Rapid Deposition of Colloidal Microspheres Flowing over Microstructured Barriers, Langmuir, 37 (2021) 6915-6922.

[20] S.Y. Jung, K.H. Ahn, Transport and deposition of colloidal particles on a patterned membrane surface: Effect of cross-flow velocity and the size ratio of particle to surface pattern, Journal of Membrane Science, 572 (2019) 309-319.

[21] L. Sicignano, G. Tomaiuolo, A. Perazzo, S.P. Nolan, P.L. Maffettone, S. Guido, The effect of shear flow on microreactor clogging, Chemical Engineering Journal, 341 (2018) 639-647.

[22] D.-C. Choi, S.-Y. Jung, Y.-J. Won, J.H. Jang, J. Lee, H.-R. Chae, K.H. Ahn, S. Lee, P.-K. Park, C.-H. Lee, Three-dimensional hydraulic modeling of particle deposition on the patterned isopore membrane in crossflow microfiltration,

Journal of Membrane Science, 492 (2015) 156-163.

[23] D. Lee, K.H. Ahn, Flow patterns in 4:1 micro-contraction flows of viscoelastic fluids, Korea-Australia Rheology Journal, 27 (2015) 65-73.

[24] B.W. Jo, A. Lee, K.H. Ahn, S.J. Lee, Evaluation of jet performance in drop-on-demand (DOD) inkjet printing, Korean Journal of Chemical Engineering, 26 (2009) 339-348.

[25] S. Chen, W. Liu, S. Li, Effect of long-range electrostatic repulsion on pore clogging during microfiltration, Physical Review E, 94 (2016) 063108.

[26] R.C. Hidalgo, A. Goñi-Arana, A. Hernández-Puerta, I. Pagonabarraga, Flow of colloidal suspensions through small orifices, Physical Review E, 97 (2018) 012611.

[27] G. Gerber, M. Bensouda, D.A. Weitz, P. Coussot, Self-Limited Accumulation of Colloids in Porous Media, Physical Review Letters, 123 (2019) 158005.

[28] E. Dressaire, A. Sauret, Clogging of microfluidic systems, Soft Matter, 13 (2017) 37-48.

[29] A.I. Cirillo, G. Tomaiuolo, S. Guido, Membrane Fouling Phenomena in Microfluidic Systems: From Technical Challenges to Scientific Opportunities, Micromachines (Basel), 12 (2021) 820.

[30] C. Duchêne, V. Filipe, S. Huille, A. Lindner, Clogging of microfluidic constrictions by monoclonal antibody aggregates: role of aggregate shape and deformability, Soft Matter, 16 (2020) 921-928.

[31] B. Mustin, B. Stoeber, Deposition of particles from polydisperse suspensions in

microfluidic systems, Microfluidics and Nanofluidics, 9 (2010) 905-913.

[32] M. Robert de Saint Vincent, M. Abkarian, H. Tabuteau, Dynamics of colloid accumulation under flow over porous obstacles, Soft Matter, 12 (2016) 1041-1050.

[33] P. Bacchin, A. Marty, P. Duru, M. Meireles, P. Aimar, Colloidal surface interactions and membrane fouling: Investigations at pore scale, Advances in colloid and interface science, 164 (2010) 2-11.

[34] Z.B. Sendekie, P. Bacchin, Colloidal Jamming Dynamics in Microchannel Bottlenecks, Langmuir, 32 (2016) 1478-1488.

[35] G.C. Agbangla, P. Bacchin, E. Climent, Collective dynamics of flowing colloids during pore clogging, Soft Matter, 10 (2014) 6303-6315.

[36] N. Delouche, A.B. Schofield, H. Tabuteau, Dynamics of progressive pore clogging by colloidal aggregates, Soft Matter, 16 (2020) 9899-9907.

[37] N. Delouche, J.M. van Doorn, T.E. Kodger, A.B. Schofield, J. Sprakel, H. Tabuteau, The contribution of colloidal aggregates to the clogging dynamics at the pore scale, Journal of Membrane Science, 635 (2021) 119509.

[38] M.T. Stamm, T. Gudipaty, C. Rush, L. Jiang, Y. Zohar, Particle aggregation rate in a microchannel due to a dilute suspension flow, Microfluidics and Nanofluidics, 11 (2011) 395.

[39] Y.K. Lee, C. Porter, S.L. Diamond, J.C. Crocker, T. Sinno, Deposition of sticky spheres in channel flow: Modeling of surface coverage evolution requires accurate sphere-sphere collision hydrodynamics, Journal of Colloid and Interface Science, 530 (2018) 383-393.

[40] M. Trofa, G. D'Avino, L. Sicignano, G. Tomaiuolo, F. Greco, P.L. Maffettone, S. Guido, CFD-DEM simulations of particulate fouling in microchannels, Chemical Engineering Journal, 358 (2019) 91-100.

[41] Y. Kim, K.H. Ahn, S.J. Lee, Clogging mechanism of poly(styrene) particles in the flow through a single micro-pore, Journal of Membrane Science, 534 (2017) 25-32.

[42] B. Dersoir, M.R. de Saint Vincent, M. Abkarian, H. Tabuteau, Clogging of a single pore by colloidal particles, Microfluidics and Nanofluidics, 19 (2015) 953-961.

[43] B. Dersoir, A.B. Schofield, M. Robert de Saint Vincent, H. Tabuteau, Dynamics of pore fouling by colloidal particles at the particle level, Journal of Membrane Science, 573 (2019) 411-424.

[44] B. Dersoir, A.B. Schofield, H. Tabuteau, Clogging transition induced by self filtration in a slit pore, Soft Matter, 13 (2017) 2054-2066.

[45] S.-H. Yoon, C.-H. Lee, K.-J. Kim, A.G. Fane, Three-dimensional simulation of the deposition of multi-dispersed charged particles and prediction of resulting flux during cross-flow microfiltration, Journal of Membrane Science, 161 (1999) 7-20.

[46] P.G. Saffman, The lift on a small sphere in a slow shear flow, Journal of Fluid Mechanics, 22 (1965) 385-400.

[47] P. Bacchin, P. Aimar, R.W. Field, Critical and sustainable fluxes: Theory, experiments and applications, Journal of Membrane Science, 281 (2006) 42-69.

[48] G.C. Agbangla, É. Climent, P. Bacchin, Experimental investigation of pore

clogging by microparticles: Evidence for a critical flux density of particle yielding arches and deposits, Separation and Purification Technology, 101 (2012) 42-48.

[49] J. Lee, H. Seo, S.-H. Park, E. Kim, J. Lee, P. Liu, S. Jeon, S. Hong, T. Kim, Tangential flow filtration of ceria slurry: Application of a single-pass method to improve buff cleaning, Materials Science in Semiconductor Processing, 145 (2022) 106618.

[50] Y.-J. Seo, S.-Y. Kim, W.-S. Lee, Advantages of point of use (POU) slurry filter and high spray method for reduction of CMP process defects, Microelectronic Engineering, 70 (2003) 1-6.

[51] V. Rastegar, G. Ahmadi, S.V. Babu, Filtration of aqueous colloidal ceria slurries using fibrous filters – An experimental and simulation study, Separation and Purification Technology, 176 (2017) 231-242.

[52] J. Park, N. Willenbacher, K.H. Ahn, How the interaction between styrene-butadiene-rubber (SBR) binder and a secondary fluid affects the rheology, microstructure and adhesive properties of capillary-suspension-type graphite slurries used for Li-ion battery anodes, Colloids and Surfaces A: Physicochemical and Engineering Aspects, 579 (2019) 123692.

[53] J.H. Park, S.H. Sung, S. Kim, K.H. Ahn, Significant Agglomeration of Conductive Materials and the Dispersion State Change of the Ni-Rich NMC-Based Cathode Slurry during Storage, Industrial & Engineering Chemistry Research, 61 (2022) 2100-2109.

[54] P. Le-Clech, V. Chen, T.A.G. Fane, Fouling in membrane bioreactors used in

wastewater treatment, Journal of Membrane Science, 284 (2006) 17-53.

[55] A.L. Lim, R. Bai, Membrane fouling and cleaning in microfiltration of activated sludge wastewater, Journal of Membrane Science, 216 (2003) 279-290.

[56] A. Hoque, K. Kimura, T. Miyoshi, N. Yamato, Y. Watanabe, Characteristics of foulants in air-sparged side-stream tubular membranes used in a municipal wastewater membrane bioreactor, Separation and Purification Technology, 93 (2012) 83-91.

[57] J. Casetta, D.G. Ortiz, C. Pochat-Bohatier, M. Bechelany, P. Miele, Atomic layer deposition of TiO2 on porous polysulfone hollow fibers membranes for water treatment, Separation and Purification Technology, 312 (2023) 123377.

[58] G. Brans, C.G.P.H. Schroën, R.G.M. van der Sman, R.M. Boom, Membrane fractionation of milk: state of the art and challenges, Journal of Membrane Science, 243 (2004) 263-272.

[59] M. Granger-Delacroix, N. Leconte, C. Grassin, F. Le Goff, F. Garnier-Lambrouin, M. Van Audenhaege, G. Gésan-Guiziou, Skimmed milk microfiltration in diafiltration mode: Impact of solvent nature and concentration factor on spiral-wound membrane performance operated at low temperature, Separation and Purification Technology, 304 (2023) 122326.

[60] C. Charcosset, Membrane processes in biotechnology: An overview, Biotechnology Advances, 24 (2006) 482-492.

[61] Y. Gao, J. Qin, Z. Wang, S.W. Østerhus, Backpulsing technology applied in MF and UF processes for membrane fouling mitigation: A review, Journal of Membrane Science, 587 (2019) 117136.

[62] J.M. Wang, Q.Q. Jin, Y.Y. Zhang, H.C. Fang, H.M. Xia, Reducing the membrane fouling in cross-flow filtration using a facile fluidic oscillator, Separation and Purification Technology, 272 (2021) 118854.

[63] Z.A. Kuznar, M. Elimelech, Direct microscopic observation of particle deposition in porous media: Role of the secondary energy minimum, Colloids and Surfaces A: Physicochemical and Engineering Aspects, 294 (2007) 156-162.

[64] J. Linkhorst, T. Beckmann, D. Go, A.J.C. Kuehne, M. Wessling, Microfluidic colloid filtration, Scientific Reports, 6 (2016) 22376.

[65] I. Bouhid de Aguiar, M. Meireles, A. Bouchoux, K. Schroën, Microfluidic model systems used to emulate processes occurring during soft particle filtration, Scientific Reports, 9 (2019) 3063.

[66] R. Makabe, K. Akamatsu, S.-i. Nakao, Mitigation of particle deposition onto membrane surface in cross-flow microfiltration under high flow rate, Separation and Purification Technology, 160 (2016) 98-105.

[67] J.H. Jang, J. Lee, S.-Y. Jung, D.-C. Choi, Y.-J. Won, K.H. Ahn, P.-K. Park, C.-H. Lee, Correlation between particle deposition and the size ratio of particles to patterns in nano- and micro-patterned membrane filtration systems, Separation and Purification Technology, 156 (2015) 608-616.

[68] K. Ohanessian, M. Monnot, P. Moulin, J.-H. Ferrasse, C. Barca, A. Soric, O. Boutin, Dead-end and crossflow ultrafiltration process modelling: Application on chemical mechanical polishing wastewaters, Chemical Engineering Research and Design, 158 (2020) 164-176.

[69] L. Song, Flux decline in crossflow microfiltration and ultrafiltration:

mechanisms and modeling of membrane fouling, Journal of Membrane Science, 139 (1998) 183-200.

[70] R. Chan, V. Chen, The effects of electrolyte concentration and pH on protein aggregation and deposition: critical flux and constant flux membrane filtration, Journal of Membrane Science, 185 (2001) 177-192.

[71] Y.-Y. Chiu, C.-K. Huang, Y.-W. Lu, Enhancement of microfluidic particle separation using cross-flow filters with hydrodynamic focusing, Biomicrofluidics, 10 (2016) 011906.

[72] K.D. Lenz, S. Jakhar, J.W. Chen, A.S. Anderson, D.C. Purcell, M.O. Ishak, J.F. Harris, L.E. Akhadov, J.Z. Kubicek-Sutherland, P. Nath, H. Mukundan, A centrifugal microfluidic cross-flow filtration platform to separate serum from whole blood for the detection of amphiphilic biomarkers, Scientific Reports, 11 (2021) 5287.

[73] R. van Zwieten, T. van de Laar, J. Sprakel, K. Schroën, From cooperative to uncorrelated clogging in cross-flow microfluidic membranes, Scientific Reports, 8 (2018) 5687.

[74] L.E. Rodd, T.P. Scott, D.V. Boger, J.J. Cooper-White, G.H. McKinley, The inertio-elastic planar entry flow of low-viscosity elastic fluids in micro-fabricated geometries, Journal of Non-Newtonian Fluid Mechanics, 129 (2005) 1-22.

[75] N.S. Martys, M. Khalil, W.L. George, D. Lootens, P. Hébraud, Stress propagation in a concentrated colloidal suspension under shear, The European Physical Journal E, 35 (2012) 20.

[76] A.P.R. Eberle, N. Martys, L. Porcar, S.R. Kline, W.L. George, J.M. Kim, P.D. Butler, N.J. Wagner, Shear viscosity and structural scalings in model adhesive hard-sphere gels, Physical Review E, 89 (2014) 050302.

[77] D. Hülagü, C. Tobias, E. Climent, A. Gojani, K. Rurack, V.-D. Hodoroaba, Generalized Analysis Approach of the Profile Roughness by Electron Microscopy with the Example of Hierarchically Grown Polystyrene–Iron Oxide–Silica Core–Shell–Shell Particles, Advanced Engineering Materials, 24 (2022) 2101344.

[78] H.M. Wyss, D.L. Blair, J.F. Morris, H.A. Stone, D.A. Weitz, Mechanism for clogging of microchannels, Physical Review E, 74 (2006) 061402.

국문 초록

복잡 유동장 내 콜로이드 현탁액의 입자 적층 및 유로 막힘 거동에 관한 연구

김대연
서울대학교 화학생물공학부

본 학위논문의 목표는 복잡 유동 하에서 나타나는 입자계 현탁액의 입자 적층과 그로 인한 유로 막힘 현상의 과정을 이해하고 메커니즘을 규명하여 막 분리 공정 등의 다양한 유동 환경에서 발생하는 적층 현상 완화에 대한 기초적인 이해를 제시하는 것이다. 막 오염의 메커니즘을 규명하고 이를 저감시키기 위해 미세유체공학 (microfluidics)을 이용한 연구들이 광범위하게 진행되어 왔지만, 대부분의 연구는 다중 공극 구조에서 현상학적 연구로 진행되었고 막을 구성하는 가장 기본 단위인 단일 공극 구조에서의 적층 환경을 이해하려는 연구는 잘 이루어지지 않았다. 따라서 본 연구에서는 막 분리 공정의 대표적인 여과 방법인 전량흐름 여과 (Dead-end flow filtration)와 교차흐름 여과 (Cross-end flow filtration)의 단위 구조를 각각 수축 (contraction) 미세 채널과 T자 (T-shaped) 미세 채널로 단순화하여 단일 공극 구조에서의 입자 적층 및 유로 막힘 현상을 분석하였다. 실제 입자 적층 현상은 입자에 작용하는 부착 및 탈착과 관련한 힘이 중요하게 작용하기 때문에 입자와 입자, 입자와 벽 간의 상호 작용과 흐름으로 인한 유체역학적 상호작용을 모두 고려하여 종합적인 적층 연구 방법론을 구성하였다.

먼저, 수축 채널에서의 염의 농도와 유동 환경에 따른 입자 적층 현상을 연구하였다. 글리세롤 수용액에 폴리스티렌 (polystyrene) 입자가 분산된 현탁액이 사용되었다. 염의 농도를 통해 콜로이드 상호작용의 크기를 조절하였고 부피 유량 조절을 통해 유체역학적 상호작용이 조절되었다. 염의 농도에 따라 수축 채널에서의 입자 적층 양상은 상이하게 변화하였다. 강한 인력의 콜로이드 상호작용을 하는 경우, 입자 적층이 주로 채널의 상류 (upstream) 영역에 발생하였지만 반발력의 콜로이드 상호작용을 하는 경우에는 주로 채널의 하류 (downstream) 영역에 적층이 발생하였다. 또한 유속이 증가할수록 더 빠르게 적층이 진행되었고, 상류 영역 적층의 양이 증가하는 것이 확인되었다. 특이한 적층 현상을 정량적으로 분석하기 위해 이미지 처리 및 내부 압력 강하를 측정되었으며, 콜로이드 상호작용 및 유체역학적 상호작용의 상대적인 크기 비교를 통해 관찰된 적층 현상이 설명되었다. 상류와 하류에서 각 상호작용으로 인한 힘의 상대적인 크기에 따라 적층의 진행 유무가 결정된다는 결론을 도출하였고, 이와 함께 콜로이드 크기로 인한 유체역학적 힘의 변화도 영향을 미치는 것을 확인하였다.

다음으로, T 자 채널에서의 흐름 조건에 따른 입자 적층 현상을 연구하였다. T 자 채널에서는 입자 적층 과정 중 탈착력으로 작용하는 흐름으로 인한 응력의 영향에 집중하였다. 유체역학적 응력은 유체의 점도와 유속에 의해 변화되며 유체의 점도는 글리세롤의 농도를 통해 조절되었다. 입자의 적층 과정은 모서리 적층, 적층의 성장, 유로 막힘의 순으로 단계적으로 진행되는 것을 확인할 수 있었다. 이 과정 중 입자가 적층된 응집체 위에서 굴러가는 듯이 보이는 롤링 (rolling) 현상과 응집체가 통째로 분리되어 흘러가는 응집체 파괴 (agglomerate breakup) 현상이 반복되었다. 입자 적층을 정량화하기 위해 공극 막힘 비

(blockage ratio)와 적층 면적 비 (deposition ratio)를 정의하였는데, 정의된 두 개의 파라미터는 특정 응력을 기준으로 경향성이 변화되었다. 이를 통해 유로 막힘을 유발하는 임계 응력 (critical stress)의 존재를 확인하였다. 임계 응력보다 작은 응력에서는 유로 막힘에 도달하며, 임계 응력보다 더 큰 응력에서는 유로 막힘이 발생하지 못하고 응력의 크기에 따라 적층이 저해되는 결과를 확인하였다. 임계 응력의 값은 유체역학적 항력과 입자간 상호작용 힘의 비로 표현되는 무차원수를 통해 유효성이 검증되었다. 또한 유로 막힘이 발생하는 응력 범위에서, 응력이 증가할수록 더 많은 수의 입자가 유로를 통과해야 비로소 유로 막힘이 발생할 수 있는 결과를 확인하였다. 이를 통해, 흐름으로 인한 응력이 입자 적층 및 유로 막힘에 매우 주요한 영향을 미칠 수 있다는 것과 부착력과 탈착력의 상대적 비가 유로 막힘을 예상하는 지표로 사용될 수 있다는 결론을 도출하였다.

본 학위논문은 복잡 유동 구조 하에서의 입자 적층 현상을 여러 힘들의 균형 관계를 통해 고찰함으로써 적층 및 유로 막힘 현상을 종합적으로 이해하는 데에 기여한다. 본 논문에서 진행된 단위 구조 채널에서의 입자 적층에 대한 고찰과 분석 방법론은 복잡 유체 및 다양한 단위 구조 채널에서의 적층 및 유로 막힘 연구에 근간을 제공할 것으로 기대되며, 이를 바탕으로 효과적인 입자 적층 및 유로 막힘 저감 전략을 수립할 수 있을 것이라 기대된다.

주요어: 입자 적층, 유로 막힘, 공극 오염, 전량흐름 여과, 교차흐름 여과, 수축관, T자 관, 입자계 현탁액, 응집, 분산, 미세유체공학

학 번: 2017-29046